

# Laminin $\gamma$ 1-dependent basement membranes are instrumental to ensure proper olfactory placode shape, position and boundary with the brain, as well as olfactory axon development

## Reviewed Preprint

Published from the original preprint after peer review and assessment by eLife.

## About eLife's process

### Reviewed preprint posted



November 13, 2023 (this version)

### Sent for peer review

September 18, 2023

### Posted to bioRxiv

July 1, 2023

P Tignard, K Pottin, A Geeverding, M Doulazmi, M Cabrera, C Fouquet, M Liffra, A Trembleau , MA Breau 

Sorbonne Université, Centre National de la Recherche Scientifique (CNRS UMR7622), Institut de Biologie Paris-Seine (IBPS), Developmental Biology Laboratory, Paris, France • Sorbonne Université, Centre National de la Recherche Scientifique (CNRS UMR8246), Inserm U1130, Institut de Biologie Paris Seine (IBPS), Neuroscience Paris Seine (NPS), Paris, France • Imaging Facility, Institut de Biologie Paris-Seine (IBPS) • Sorbonne Université, Centre National de la Recherche Scientifique (CNRS UMR8256), Institut de Biologie Paris Seine (IBPS), Adaptation Biologique et Vieillesse, Paris, France • Institut National de la Santé et de la Recherche Médicale (INSERM)

 [https://en.wikipedia.org/wiki/Open\\_access](https://en.wikipedia.org/wiki/Open_access)

 Copyright information

## Abstract

Despite recent progress, the complex roles played by the extracellular matrix in development and disease are still far from being fully understood. Here, we took advantage of the zebrafish *sly* mutation which affects Laminin  $\gamma$ 1, a major component of basement membranes, to explore its role in the development of the olfactory system. Following a detailed characterisation of Laminin distribution in the developing olfactory circuit, we analysed basement membrane integrity, olfactory placode and brain morphogenesis, and olfactory axon development in *sly* mutants, using a combination of immunochemistry, electron microscopy and quantitative live imaging of cell movements and axon behaviours. Our results point to an original and dual contribution of Laminin  $\gamma$ 1-dependent basement membranes in organising the border between the olfactory placode and the adjacent brain: they maintain placode shape and position in the face of major brain morphogenetic movements, they establish a robust physical barrier between the two tissues while at the same time allowing the local entry of the sensory axons into the brain and their navigation towards the olfactory bulb. This work thus identifies key roles of Laminin  $\gamma$ 1-dependent basement membranes in neuronal tissue morphogenesis and axon development *in vivo*.

### eLife assessment

This is an **important** study describing the function of Laminin  $\gamma$ 1-dependent basement membranes in the development of the olfactory placode, including morphogenesis of the placode, boundary formation, and olfactory axonal pathfinding. The study uses elegant live imaging approaches, and detailed mutant analyses to provide a **convincing** description of the role of Laminin in olfactory placode development, although the mechanisms by which Laminin  $\gamma$ 1 regulates these processes are not conclusive. In addition to the contributions this study makes to understanding olfactory placode development, it will also be of broader interest to individuals interested in extracellular matrix regulation of tissue morphogenesis, and neural development including neuronal pathfinding.

## Introduction

The extracellular matrix (ECM) is a network of glycoproteins which provides support to tissues by contributing to mechanical and chemical signals regulating their biology. It regulates multiple processes, including cell migration, survival/proliferation, differentiation and polarity (Walma and Yamada, 2020 [↗](#)). In addition to the fundamental role of ECM in development and homeostasis, mutations in matrix genes lead to a variety of genetic disorders, and abnormal ECM remodelling drives disease progression in fibrosis, neurological disorders and cancer (Karamanos et al., 2021 [↗](#); Soleman et al., 2013 [↗](#); Theocharis et al., 2019 [↗](#); Yamada et al., 2022 [↗](#)). ECM components are also critical factors in tissue engineering and regenerative medicine (Kaur et al., 2021 [↗](#); Kim et al., 2021 [↗](#)), and thus represent valuable targets but also key players in a plethora of therapeutic applications.

The ECM can influence development and disease in many ways, and despite recent advances, the full complexity of ECM functions is far from being understood. This partly comes from the lack of tools to investigate ECM roles *in vivo*. Indeed, loss-of-function of ECM components often leads to embryonic lethal phenotypes, for instance during implantation and gastrulation in mice (see for example Miner and Yurchenco, 2004 [↗](#)), precluding the analysis of ECM functions at later stages of development.

Laminins are major components of the basement membrane (BM), a layer of ECM lying on the basal side of epithelia, which is essential for their development and homeostasis. Laminins are crucial to initiate BM assembly (Anderson et al., 2009 [↗](#); Huang et al., 2003 [↗](#); Miner and Yurchenco, 2004 [↗](#); Urbano et al., 2009 [↗](#)). They are  $\alpha/\beta/\gamma$  heterotrimers, with Laminin 111 believed to be the predominant isoform during early development (Miner and Yurchenco, 2004 [↗](#)). The zebrafish *sly*<sup>wi390</sup> (*sleepy/lamc1*) mutation (Wiellette et al., 2004 [↗](#)) affects Laminin  $\gamma$ 1, present in 10 out of 18 isoforms. *sly* homozygous mutants exhibit defects in notochord, blood vessel and somite morphogenesis (Dolez et al., 2011 [↗](#); Odenthal et al., 1996 [↗](#); Parsons et al., 2002 [↗](#); Pollard et al., 2006 [↗](#); Stemple et al., 1996 [↗](#)). Maternal or residual expression of the  $\gamma$ 1 chain until around 12 hpf (hours-post-fertilisation) (Dolez et al., 2011 [↗](#); Parsons et al., 2002 [↗](#)) likely allows *sly* mutants to develop until 48-72 hpf, thus providing an *in vivo* setting to examine later functions of this ECM component.

In this study, we took advantage of the *sly* mutant to investigate the role of Laminin  $\gamma$ 1 in the development of the zebrafish olfactory system, which forms through the growth of the axons from the olfactory placode (OP) to the olfactory bulb in the brain (Miyasaka et al., 2007 [↗](#)) in the context of morphogenetic movements shaping the OP and nearby tissues (Aguillon et al., 2020 [↗](#); Breau et

al., 2017 [↗](#); Hauptmann and Gerster, 2000 [↗](#); Monnot et al., 2022 [↗](#); Ross et al., 1992 [↗](#)). Laminin-rich BMs are known to surround the developing OPs and adjacent brain (Torres-Paz and Whitlock, 2014 [↗](#); Torres-Paz et al., 2021 [↗](#)), but their function in the construction of the olfactory system remains uncharacterised.

Laminin stimulates neurite outgrowth for many types of neurons *in vitro* (reviewed in Powell and Kleinman, 1997 [↗](#)). *In vivo*, in the developing nervous system, Laminin is important for neuro-epithelial morphogenesis (Bryan et al., 2016 [↗](#); Ivanovitch et al., 2013 [↗](#); Sidhaye and Norden, 2017 [↗](#); Tsuda et al., 2010 [↗](#)), neuronal migration (Belvindrah et al., 2007 [↗](#); Chen et al., 2009 [↗](#); Grant and Moens, 2010 [↗](#); Sittaramane et al., 2009 [↗](#)) and multiple aspects of axonal development including axon emergence (Moore et al., 2022 [↗](#); Randlett et al., 2011 [↗](#); Wolman et al., 2008 [↗](#)), growth, and pathfinding (Bonner and O'Connor, 2001 [↗](#); Chen et al., 2009 [↗](#); García-Alonso et al., 1996 [↗](#); Karlstrom et al., 1996 [↗](#); Paulus and Halloran, 2006 [↗](#)).

Here, we provide a detailed characterisation of Laminin expression during the construction of the zebrafish olfactory system, in fixed and live embryos. We then use the *sly* mutant, combined with live imaging to quantify cell/tissue movements and axon behaviours, to investigate Laminin  $\gamma$ 1 functions in neuronal tissue morphogenesis and axon development *in vivo*. We found that Laminin  $\gamma$ 1-dependent BMs are instrumental to maintain proper OP morphology and position, to define the boundary between the OP and the brain and to allow the growth and pathfinding of the axons towards the olfactory bulb.

## Results

### The developing OP and brain tissues are surrounded by Laminin-containing BMs

We first analysed Laminin distribution during early OP morphogenesis. Between 14 and 22 hpf, in a process referred to as OP coalescence, cell movements transform the elongated OP domains into two rounded placodal structures on each side of the brain (Whitlock and Westerfield, 2000 [↗](#)). This occurs through two cell movements: first, cell bodies from the anteroposterior extremities of the OP domain converge towards the OP centre. OP cell bodies then move laterally, away from the brain, while their trailing axons remain attached to the brain and grow through retrograde extension (Aguillon et al., 2020 [↗](#); Breau et al., 2017 [↗](#); Monnot et al., 2022 [↗](#)). During OP coalescence, cells in the adjacent brain undergo a directional anterior movement (Breau et al., 2017 [↗](#); Monnot et al., 2022 [↗](#)). To analyse Laminin expression at these stages, we performed immunostainings with a Laminin 111 polyclonal antibody on *Tg(neurog1:GFP)* embryos (Blader et al., 2003 [↗](#)), in which the early-born OP neurons and a subpopulation of forebrain cells are labelled with GFP (Aguillon et al., 2020 [↗](#); Breau et al., 2017 [↗](#); Madelaine et al., 2011 [↗](#)). Consistent with previous observations (Torres-Paz and Whitlock, 2014 [↗](#); Torres-Paz et al., 2021 [↗](#)), we first noticed the appearance of a continuous Laminin-rich BM surrounding the brain from 14–18 hpf, while around the OP, only discrete Laminin spots were detected at this stage (**Fig. 1A, A'** [↗](#)). By contrast, at the end of coalescence (22 hpf), two distinct BMs were clearly visible, one around the brain and the other one partially enveloping the OP (**Fig. 1B, B'** [↗](#)), suggesting that the Laminin-rich BM of the OP assembles between 18 and 22 hpf, during the late phase of OP coalescence.

To further analyse the dynamics of Laminin  $\gamma$ 1 expression and BM assembly during OP coalescence, we took advantage of the *TgBAC(lamC1:lamC1-sfGFP)* line, in which Laminin  $\gamma$ 1 is tagged with superfolder GFP and expressed under the control of its own promoter (Yamaguchi et al., 2022 [↗](#)). To co-label OP cells, we used the *Tg(cldnb:Gal4; UAS:RFP)* line (Breau et al., 2013 [↗](#)), which expresses RFP in OP cells and in the periderm from around 16 hpf. RFP expression is initially weak and mosaic (**Fig. 1E** [↗](#)) and becomes progressively stronger and widespread in the

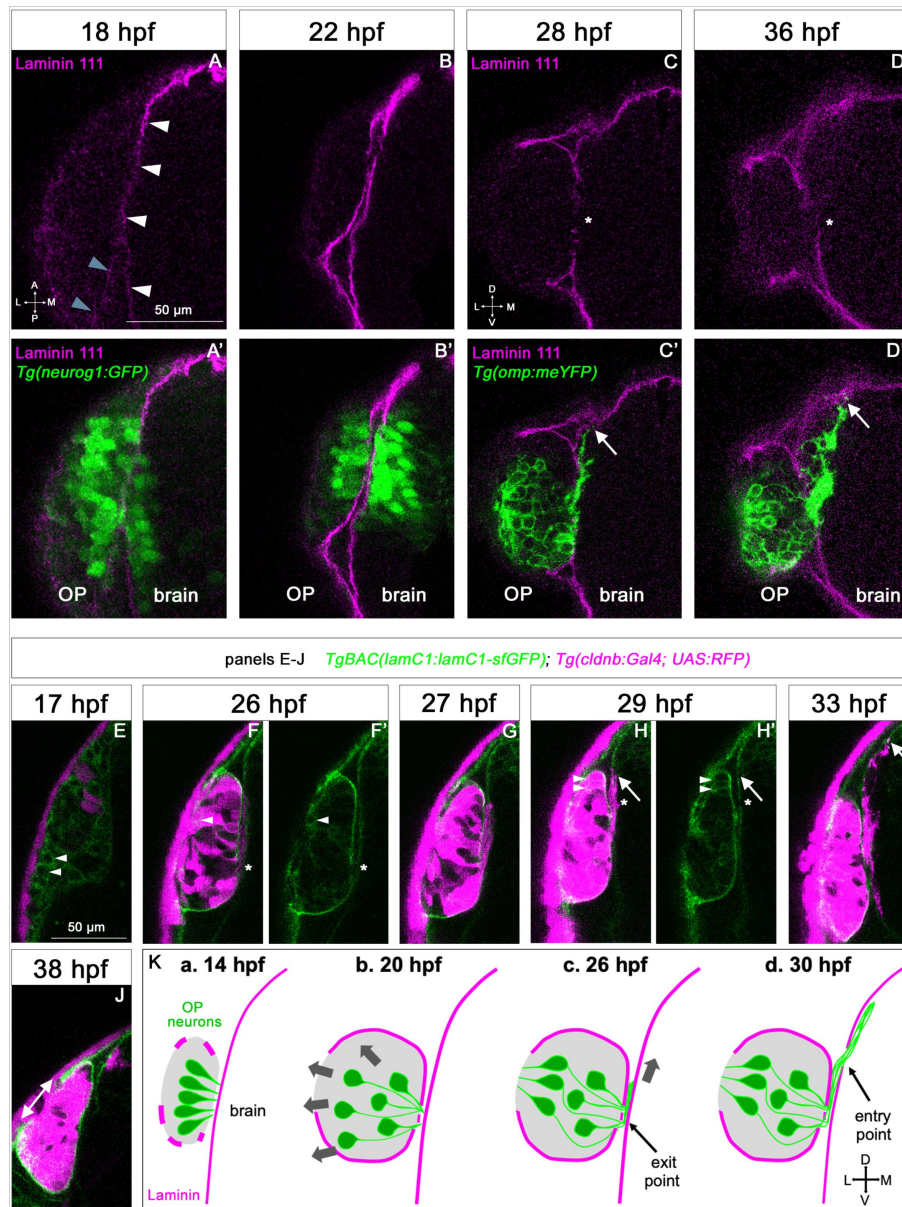


**Figure 1.**

### Expression profile of Laminin in relation with the development of the olfactory system.

**A-D.** Immunostaining for Laminin 111 (magenta) on *Tg(neurog1:GFP)* embryos (green) at 18 and 22 hpf (A-B', dorsal views), and on *Tg(omp:meYFP)* embryos (green) at 28 and 36 hpf (C-D', frontal views). In A, white arrowheads = BM-like Laminin staining around the brain, grey arrowheads = spotty Laminin accumulation around the OP. In C-D', asterisks = interruptions in the OP's and brain's BM where the YFP+ axons exit the OP and enter the brain. arrows = distalmost extremity of the YFP+ axon bundle, which is in close contact with the internal side of the brain's BM. **E-J.** Images extracted from confocal live imaging on *TgBAC(lamC1:lamC1-sfGFP); Tg(cldnb:Gal4; UAS:RFP)* embryos (frontal view). LamC1-sfGFP expression in green, and RFP expression (OP cells and peridermal skin cells) in magenta. Arrowheads = OP cells with cytoplasmic LamC1-sfGFP accumulation. Asterisks in F and H = axon exit point and entry point, respectively. Arrows in H and I = distalmost extremity of the RFP+ axon bundle, located close to the brain's BM. In J, double headed arrow = gap in the LamC1-sfGFP observed at the interface with the periderm, where the nostril orifice opens in the skin, as previously reported (Baraban et al., 2023). **K.** Schematic representation of Laminin-containing BM (magenta) assembly during OP coalescence (a, b), of the formation of the exit/entry points (b, d) and the associated axonal behaviours: retrograde axon extension in the OP in b, growth as a fasciculated bundle, initially between the BMs of the OP and the brain (c), and then along the internal side of the brain's BM (d). Scale bar: 50  $\mu$ m.



OP (**Fig. 1F**). Using confocal live imaging ( $n = 4$  imaged embryos, 2 independent experiments), we confirmed the progressive BM-like accumulation of LamC1-sfGFP around the OP, with a gradual increase of the BM fluorescence during OP coalescence (**Fig. 1E-F'** and Movie 1). From 14 hpf, mesenchymal cells exhibiting cytoplasmic Laminin-sfGFP were seen to migrate anteriorly around the OP (Movie 1). According to the literature, these cells could represent neural crest cells (NCC) (Bryan et al., 2020; Harden et al., 2012; Torres-Paz and Whitlock, 2014) and/or mesodermally-derived cells of the periocular mesenchyme (Vöcking et al., 2023). A subset of RFP+ OP cells also displayed cytoplasmic Laminin-sfGFP (**Fig. 1E-H'** and Movie 1). Altogether, these live imaging experiments suggest that Laminin  $\gamma 1$  around the OP is deposited mostly during late coalescence stages, from at least a subset of OP cells and surrounding mesenchymal cells. Telencephalic cells also exhibited cytoplasmic Laminin-sfGFP expression throughout OP coalescence (Movie 2), suggesting that the forebrain contributes to the deposition of its own Laminin  $\gamma 1$ -containing BM at these stages.

To analyse whether the BMs of the brain and OP tissues are maintained at later stages, we used Laminin immunostaining on *Tg(omp:meYFP)* embryos, in which a subpopulation of OP neurons is labelled from 22-24 hpf (Miyasaka et al., 2005; Miyasaka et al., 2007; Sato et al., 2005; Sato et al., 2007), and confocal live imaging with the LamC1-sfGFP reporter line. Using both approaches we observed a strong, continuous BM-like signal enveloping the brain and the OP at these stages, except (i) where the olfactory axons leave the OP and enter the brain (defined respectively as the exit and entry points, see below) and, as we previously reported (Baraban et al., 2023), (ii) above of the neuronal rosette assembling in the dorso-lateral OP, where the nostril orifice opens in the skin (**Fig. 1C-D', 1G-J**). Thus, the OP and adjacent brain tissues are ensheathed by BMs from early stages of olfactory system assembly (as depicted in **Fig. 1K**), suggesting these BMs could play a role in their morphogenesis or the maintenance of their shape during development.

## Laminin distribution suggests a role in olfactory axon development

It has been proposed that the zebrafish OP contains a transient population of pioneer neurons in the ventro-medial region of the OP: their axons are the first to grow out of the OP at 22-24 hpf, and ablation experiments suggest that they act as a scaffold for the growth of the axons of the later born olfactory sensory neurons (OSNs), located in the dorso-lateral rosette (Whitlock and Westerfield, 1998). To investigate the distribution of Laminin in relation with axonal development, we used the *Tg(omp:meYFP)* line to visualise olfactory axons, including pioneer axons and axons from the ciliated OSNs (Miyasaka et al., 2005; Miyasaka et al., 2007). Previous time-course studies using this line showed that following OP coalescence, the YFP+ axons leave the OP from 22-24 hpf through a restricted region in the ventro-medial OP (the exit point), grow dorsally as a fasciculated bundle until around 32 hpf, then start defasciculating in the presumptive olfactory bulb region in the brain (reviewed in Breau and Trembleau, 2023; Miyasaka et al., 2005; Miyasaka et al., 2007; Sato et al., 2007). Immunostaining for Laminin 111 revealed local disruptions in the BMs ensheathing the OP and the brain, precisely where the YFP+ axons exit the OP (exit point) and enter the brain (entry point) (**Fig. 1C-D'**). Once into the brain, from around 28 hpf, the most distal extremity of the YFP+ axon bundle was systematically in close contact with the Laminin-labelled BM of the brain (**Fig. 1C-D'**), suggesting that the growth cones use it as a substrate to migrate towards the olfactory bulb.

To better understand when and how the gaps of the exit and entry points form in the BMs, we took advantage of our live imaging experiments performed on *TgBAC(lamC1:lamC1-sfGFP); Tg(cldnb:Gal4; UAS:RFP)* embryos. By the end of the coalescence, during the assembly of the BM around the OP, we noticed that small interruptions of the BM were already present near the axon tips, along the ventro-medial wall of the OP (Movie 2). This suggests that the exit point does not open through local perforation of a pre-existing BM around the OP but through incomplete BM

synthesis/assembly in this area. The entry point was slightly more dorsal than the exit point (of about 10–20  $\mu\text{m}$ ), and the initial dorsal growth of the axons thus occurred between the two BMs (**Fig. 1F–H'**). The opening of the entry point through the brain BM was concomitant with the arrival of the RFP+ axons, suggesting that the axons degrade or displace BM components to enter the brain (**Fig. 1G–H'** and Movie 2). Once in the brain, as observed in fixed embryos, the distal tip of the RFP+ axons migrated in close proximity with the brain's BM (**Fig. 1H, I**). Overall our observations indicate that the axons first grow dorsally for a short distance between the BMs of the OP and the brain, and then migrate along the internal side of the brain's BM (**Fig. 1K**). We thus hypothesise that the Laminin-rich BMs serve as a migratory path for the axons during their journey from the OP to the olfactory bulb.

## The integrity of BMs around the brain and the OP is affected in the *sly* mutant

We used the *sly* mutant to analyse the function of Laminin  $\gamma 1$  in the development of the zebrafish olfactory system. As previously observed (Dolez et al., 2011; Parsons et al., 2002; Stemple et al., 1996; Wielllette et al., 2004), Laminin 111 BM-like accumulation could not be detected in *sly*<sup>−/−</sup> mutants (referred to as *sly* mutants) at all the analysed stages, from 16 to 36 hpf, while heterozygous *sly*<sup>+/-</sup> embryos displayed an expression pattern that was similar to *sly*<sup>+/+</sup> embryos (**Fig. 2A–C'**). This indicates that the  $\gamma 1$  chain is required for the assembly of Laminin 111, and that there is likely no residual/maternal Laminin at the onset of OP coalescence. Since Laminins are essential for BM assembly in other contexts (Lee and Gross, 2007; Li et al., 2005; Miner and Yurchenco, 2004; Smyth et al., 1999; Urbano et al., 2009), we further checked the presence and structure of the BMs in *sly* mutants. We carried out immunostaining for two other BM components, Collagen IV and Nidogen, at 22, 28 and 36 hpf. Nidogen was present in BM-like structures around the OP and the brain in control siblings, with a pattern resembling that of Laminin 111, while in *sly* mutants no BM staining could be detected around the two tissues (**Fig. 2D–F'**). In controls, Collagen IV was present in the linear BMs around the OP and the brain, and, with a more fibrous distribution, in the mesenchymal tissues surrounding the OP. In *sly* mutants, Collagen IV immunoreactivity was not totally abolished: the BM-like staining was absent, but patches of fibrous expression remained around the OP, at various locations (**Fig. 2G–I'**).

We next used electron microscopy (EM) to analyse the ultrastructure of BMs in *sly* mutants and control siblings. We focused on the interface between the forebrain and the OP, where NCC are known to migrate during OP coalescence (Bryan et al., 2020; Harden et al., 2012; Torres-Paz and Whitlock, 2014). NCC, OP and brain cells could be identified on the large field EM images by their position and morphology (**Fig. 2L, L'**). At 24 hpf in controls, the plasma membranes of NCC were separated from those of adjacent OP and brain cells by a 120 nm-wide gap containing electron dense ECM material (**Fig. 2J, M**). This material likely represents the BMs of the two tissues, with morphological features resembling those of BMs found in other tissues of zebrafish embryos at similar stages (Bryan et al., 2020; Yamaguchi et al., 2022). In *sly* mutants, almost no NCC could be detected, suggesting that NCC development is affected. In this mutant context, the plasma membranes of OP and brain cells were separated by a 40 nm-wide gap, which was significantly smaller than in controls. This gap was most often devoid of electron dense material (**Fig. 2J, J', M**). A similar trend was detected at 32 hpf (**Fig 2K, K', N**). By contrast, the thickness of the intercellular gaps within the OP or the brain was not affected in mutants (Fig. S1). The integrity of the OP and brain BMs is thus strongly affected in *sly* mutants, as previously reported in other tissues of Laminin  $\gamma 1$  mutants (Urbano et al., 2009; Yamaguchi et al., 2022). We next analysed the consequences on the development of the olfactory system components (placode, brain, olfactory axons).

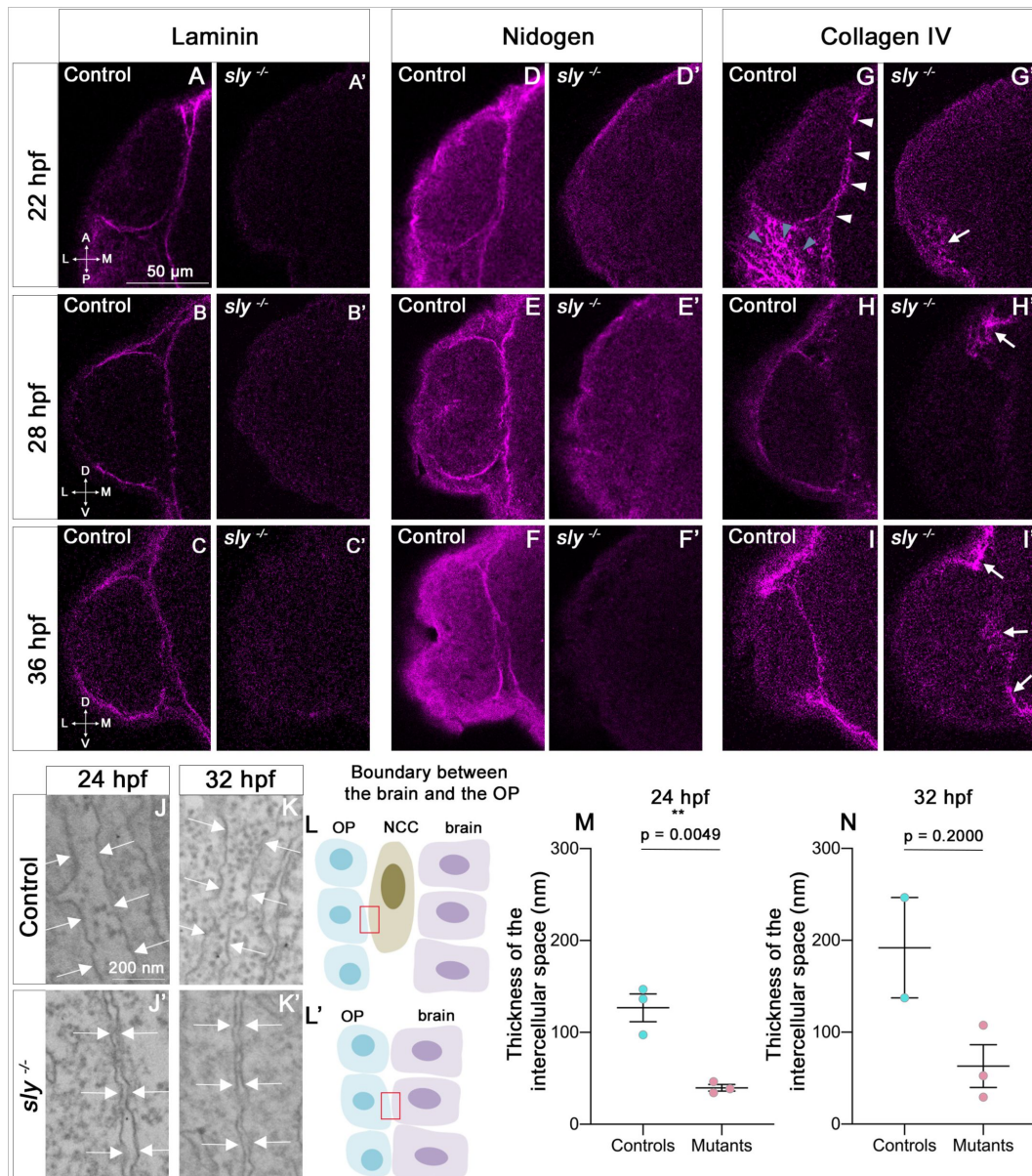


**Figure 2.**

### The integrity of the BMs of OP and brain tissues is strongly affected in *sly* mutants.

**A-I.** Immunostaining for Laminin (A-C), Nidogen (D-F) and Collagen IV (G-I) on *sly* mutants and control siblings at 22 (dorsal view), 28, and 36 hpf (frontal view). For Laminin and Nidogen, the linear, BM-like staining seen in controls around the OP and brain tissues is not detected in *sly* mutants. In G, white arrowheads = BM-like Collagen IV staining, grey arrowheads = fibrous staining around the OP. In *sly* mutants, some fibrous patches of Collagen IV remain around the OP (arrows in G', H', I'). Scale bar: 50  $\mu$ m. **J, K.** Examples of EM images of the intercellular space between NCC and the OP in control siblings (J, K) and the OP and the brain in *sly* mutants (J', K'), at 24 (J, J') and 32 hpf (K, K'). Arrows = plasma membranes. The pictures were taken in the areas depicted with red boxes in L, L'. **L.** Schematic view of the brain/OP boundary and of the areas (red boxes) where the pictures were taken in controls (L) and *sly* mutants (L'). OP, brain and NCC were identified by their position and shape: migrating NCC showed an elongated morphology along the AP axis, which differed from the round OP cell bodies and from brain neuroepithelial cells elongated along the ML axis. **M, N.** Thickness of the intercellular space in *sly* mutants (between OP and brain cells) and control siblings (between NCC and brain or OP cells) at 24 hpf (n = 3 controls; n = 3 mutants) and 32 hpf (n = 2 controls; n = 3 mutants). For 24 hpf, unpaired, two-tailed t test. For 32 hpf, Mann-Whitney test.

## Role of Laminin $\gamma$ 1-dependent BMs in OP coalescence

To study the role of Laminin  $\gamma$ 1-dependent BMs in OP coalescence, we first measured the dimensions of the *Tg(neurog1:GFP)*<sup>+</sup> OP cell clusters at 22 hpf (end of coalescence) on fixed *sly* mutants and control siblings. While no difference was found for anteroposterior (AP) and dorsoventral (DV) dimensions, the mediolateral (ML) dimension was increased in mutants (**Fig. 3A-E**). This could be the consequence of an increased number of GFP<sup>+</sup> cells, however no difference was found in the number of mitotic cells in the OPs of *sly* mutants and control siblings at 16 and 21 hpf (Fig. S2A, B, E, F) and, as previously reported in other tissues (Parsons et al., 2002), we observed a tendency for the *sly* mutants to exhibit increased apoptosis (Fig. S2I, J, M, N). The higher ML dimension could also be due to increased lateral movements of OP cell bodies in the absence of the BM surrounding the OP. To test this, we performed live imaging on *sly* mutants and control siblings carrying the *Tg(neurog1:GFP)* transgene, mounted in a dorsal view ( $n = 5$  mutants and  $n = 5$  controls) (**Fig. 3F-I** and Movie 3). Individual nuclei of GFP<sup>+</sup> OP and brain cells were tracked using widespread expression of H2B-RFP, obtained through mRNA injection. From the cell trajectories we extracted the 3D Mean Square Displacements (MSD), a measure of the volume explored by a cell in a given period of time. No significant difference was observed for the MSD of OP cells between controls and *sly* mutants, but the MSD was higher for brain cells in the mutants (**Fig. 3J, K**). Direction wise, surprisingly OP cells did not show any change in their total ML displacement (**Fig. 3L**), nor in their DV displacement (**Fig. 3M**). Differences, although not statistically significant, could be detected along the AP axis for anterior, central and posterior OP cells: in the mutants the anterior cohort of cells tended to migrate less posteriorly, while central and posterior cells migrated more anteriorly, as if the final cell positions were all shifted towards more anterior locations (**Fig. 3N-P**). In conclusion, while the movements of brain cells are increased in the absence of BMs at coalescence stages, overall the OP cell movements occur with normal parameters and allow the condensation of OPs into compact neuronal clusters in the *sly* mutants. It is possible however that the position of the OP along the AP axis is shifted anteriorly at the end of OP coalescence.

## Role of Laminin $\gamma$ 1-dependent BMs during the forebrain flexure

Following OP coalescence, the forebrain flexure, a major morphogenetic process which is essential for the final folded shape of the vertebrate brain, starts to remodel the head tissues (Chapman et al., 2005; Garcia et al., 2017; Hauptmann and Gerster, 2000; Tropepe and Sive, 2003). In zebrafish the bending of the forebrain has been reported to occur between 24 and 48 hpf through the observation of fixed samples (Ross et al., 1992; Hauptmann and Gerster, 2000). We set out to investigate the role of the brain and OP BMs during the forebrain flexure. The *Tg(omp:meYFP)* transgene expression was used to quantify the dimensions of the YFP<sup>+</sup> cluster in the OP at various stages of the flexure (24, 28, 32 and 36 hpf). While no change could be detected in the AP and ML dimensions of the YFP<sup>+</sup> cluster, its DV dimension was significantly increased in *sly* mutants at all the analysed stages (**Fig. 4A-E** and Fig. S3A-L). This higher DV dimension is unlikely to result from an increase in the number of cells, since YFP<sup>+</sup> mitotic cells were not more numerous in *sly* mutants (Fig. S2C, D, G, H), and YFP<sup>+</sup> OP clusters displayed increased apoptosis, as observed at earlier stages (Fig. S2K, L, O, P). Counting the YFP<sup>+</sup> cells on high magnification images of 3 mutant and 3 control OPs at 28 and 36 hpf further confirmed that the YFP<sup>+</sup> cell number is unchanged (Fig. S2Q, R). In addition to the DV elongation of the OP tissue, isolated, ectopic (mispositioned) YFP<sup>+</sup> cells were observed all around the YFP<sup>+</sup> cluster in the *sly* mutants (**Fig. 4F-H** and Movie 6). The rosette structure appeared to form normally on the dorso-lateral region of the OP in *sly* mutants (Movie 6).

To better understand the origin of these phenotypes, we analysed the dynamic behaviours of brain and OP cells occurring during the forebrain flexure, which had not been characterised so far. We carried out live imaging from 22 to 40 hpf on *Tg(omp:meYFP)* *sly* mutants and control siblings injected with H2B-RFP mRNA to label all nuclei, and tracked YFP<sup>+</sup> OP cells and adjacent



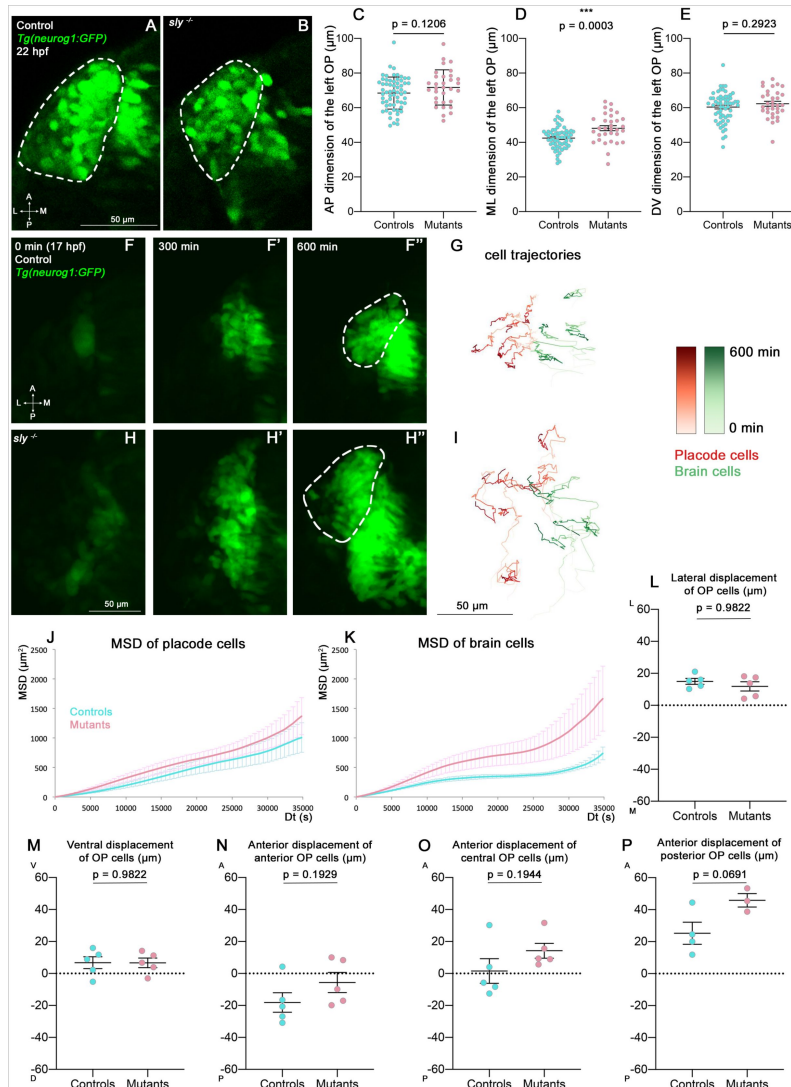


**Figure 3.**

### Analysis of OP coalescence in *sly* mutants and control siblings.

**A, B.** Images (dorsal views, 1 z-section) of representative OPs from a *Tg(neurog1:GFP); sly<sup>-/-</sup>* mutant (right) and a control *Tg(neurog1:GFP)* sibling (left) at the end of OP coalescence (22 hpf). The *Tg(neurog1:GFP)<sup>+</sup>* OP clusters are surrounded by dotted lines. **C-E.** Graphs showing the anteroposterior (AP, in C), the mediolateral (ML, in D), and dorsoventral (DV, in E) dimensions of the *Tg(neurog1:GFP)<sup>+</sup>* OP clusters in *sly* mutants (pink) and control siblings (blue) at 22 hpf ( $n = 62$  controls and  $n = 32$  mutants from 2 independent experiments). Unpaired, two-tailed t test. **F-F'' and H-H''.** Images extracted from confocal live imaging on *Tg(neurog1:GFP)* control (F-F'') and *sly* mutant (H-H'') embryos during OP coalescence, dorsal view, average projection. **G, I.** Examples of 2D tracks (ML along X and AP along Y) of *Tg(neurog1:GFP)<sup>+</sup>* OP cells (red) and *Tg(neurog1:GFP)<sup>+</sup>* brain cells (green) in a control (G) and a *sly* mutant embryo (I). The time is color-coded: light colors at the beginning of the trajectory (17 hpf) towards dark colors for the end of the track (600 min later). **J, K.** MSD analysis for OP cells (J) and brain cells (K) in *sly* mutants and control siblings ( $n = 5$  controls and  $n = 5$  mutants from 3 independent experiments, 10 to 14 cells analysed in each tissue). **L, M.** Graphs showing the total lateral (L) and ventral (M) displacement of OP cells, starting at 17 hpf and during 600 min of time lapse ( $n = 5$  control placodes and  $n = 5$  mutant placodes from 3 independent experiments, 10 to 14 cells per placode, unpaired, two-tailed t test). **N-P.** Graphs showing the total anterior displacement of anterior, central and posterior OP cells (as defined in Breau et al., 2017), starting at 17 hpf and during 600 min of time lapse ( $n = 5$  control placodes and  $n = 5$  mutant placodes from 3 independent experiments, mean calculated from 1 to 12 cells per placode, unpaired, two-tailed t test). Note that in some of the OPs we could not find any trackable (i.e. expressing H2B-RFP) posterior OP cell, which explains why there are only 4 control points and 3 mutant points in the graph showing the anterior displacement of posterior cells).

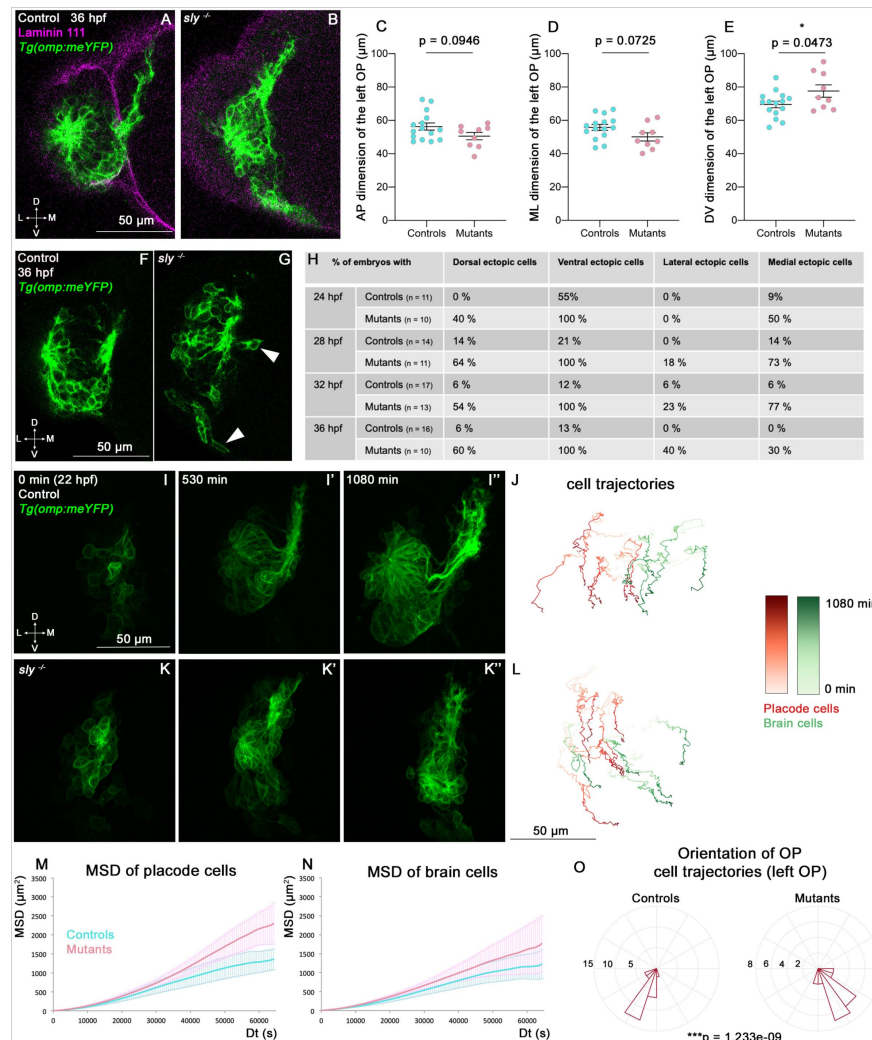


**Figure 4.**

### Analysis of OP and brain morphogenesis in *sly* mutants and control siblings during the forebrain flexure.

**A, B.** Images (frontal view, 1 z-section) of representative placodes from a *Tg(omp:meYFP); sly<sup>-/-</sup>* mutant (right) and a control *Tg(omp:meYFP)* sibling (left) at 36 hpf. Laminin immunostaining in magenta. **C-E.** Graphs showing the anteroposterior (AP, in C), the mediolateral (ML, in D), and dorsoventral (DV, in E) dimensions of the *Tg(omp:meYFP)<sup>+</sup>* OP clusters in *sly* mutants (pink) and control siblings (blue) at 36 hpf (n = 15 controls and n = 9 mutants from 4 independent experiments). Unpaired, two-tailed t test. Similar measurements performed at younger stages are shown in Fig. S3A-L. **F, G.** Examples of images used for the analysis of ectopic cells, defined as *Tg(omp:meYFP)<sup>+</sup>* cells being physically separated from the main YFP+ cluster. Arrowheads show instances of ectopic cells in a *sly* mutant. **H.** Table showing the % of control and mutant embryos with at least one ectopic cell located dorsally, ventrally, laterally, and medially to the main YFP+ cluster. The numbers of analysed embryos are indicated in the table. **I-I'' and K-K''.** Images extracted from confocal live imaging on *Tg(omp:meYFP)* control (I-I'') and *sly* mutant (K-K'') embryos during the forebrain flexure, from 22 hpf and over 1080 min, frontal view, maximum projection. **J, L.** Examples of 2D tracks (ML along X and DV along Y) of *Tg(omp:meYFP)<sup>+</sup>* OP cells (red) and adjacent brain cells (green) in a control (J) and a *sly* mutant (L). The time is color-coded: light colors at the beginning of the trajectory (22 hpf) towards dark colors for the end of the track (1080 min later). **M, N.** 3D MSD analysis of OP (M) and brain cells (N) in *sly* mutants and control siblings (n = 4 controls and n = 3 mutants from 5 independent experiments, 10 to 14 cells analysed in each tissue). **O.** Rose plots indicating the orientation of the movement for control and mutant left OP cells (data pooled from n = 4 controls and n = 3 mutants from 5 independent experiments). Numbers = number of cells. Dorsal to the top, lateral to the left. There is a statistical difference in cell track orientations between controls and mutants (circular analysis of variance based on the likelihood ratio test: p = 1.233e-09 for the left OPs, and p = 3.439e-08 for the right OPs, the graphs for the right OPs are not shown).

brain cells ( $n = 4$  mutants and  $n = 4$  controls) (Fig. 4I-L and Movie 4). From 24-26 hpf we observed a marked anterior and ventral departure of brain cells in control embryos, representing the onset of the flexure movement. Strikingly, OP cells also moved anteriorly and ventrally from these stages, in coordination with the brain, revealing that the OPs are also subjected to the flexure movement (Fig. 4J and Fig. S3M). The flexure movements were also visible in the brain and OPs of *sly* mutants (Fig. 4L and Fig. S3N), with OP cells moving with a higher MSD than in controls (Fig. 4M). A similar trend was observed for brain cells, but was not statistically significant (Fig. 4N). Moreover, upon visualisation of the cell trajectories in a lateral (YZ) view, we noticed that in 4/4 mutant embryos, brain and OP cells exhibited curved trajectories, moving first anteriorly and ventrally, then turning posteriorly, while this phenomenon occurred in only 1/4 control sibling during the duration of our movies (Fig. S3M, N). This reinforces the idea that brain and OP cells are subjected to an accelerated or enhanced forebrain flexure remodelling in the *sly* mutants, and suggests that in the wild type situation the BMs allow the tissues, and in particular the OP, to resist to the morphogenetic movements associated with the flexure. Altogether, our findings show that the Laminin  $\gamma 1$ -containing BMs are required to prevent OP cell scattering, maintain OP shape and dampen OP cell movements during the forebrain flexure.

## Laminin $\gamma 1$ -dependent BMs are required to define a robust boundary between the OP and the brain

OP cells undergo anterior and ventral movements during the forebrain flexure. We noticed that, while in control siblings OP cells also display a lateral displacement, they rather move in the medial direction in *sly* mutants, towards the brain, as if the two OPs were progressively converging towards each other (Fig. 4J, L, O). This prompted us to image OP and brain tissues in 3D to visualise the boundary between the two tissues and analyse the width of the brain. To do so, we first performed immunostainings at 28 and 36 hpf for the pan-neuronal marker HuC to visualise neurons in the OP and brain on *Tg(cldnb:Gal4; UAS:RFP)* embryos, in which RFP is expressed in the OP. Qualitative observations of these z-stacks revealed that OPs in *sly* mutants are partially embedded within the brain tissue and display a curved and irregular boundary with the brain, while the frontier between the two tissues appears as a straight line in control siblings (Fig. 5A, A', Fig. S4A, A' and Movie 5). To quantify the width of the brain, we used the *Tg(eltC:GFP)* line (Stedman et al., 2009), which expresses GFP in forebrain cells, and crossed it with the *Tg(cldnb:Gal4; UAS:RFP)* line to label the OPs (Fig. 5B, B' and Fig. S4B, B'). We measured the width of the forebrain in 3 distinct AP levels and 3 distinct DV levels in between the two OPs (as depicted in Fig. 5B, B' and Fig. S4B, B' for the DV levels). The width of the forebrain in *sly* mutants was smaller than in controls, in particular in anterior and dorsal areas (Fig. 5B-D and Fig. S4B-D). Proliferation was unchanged in the brain of *sly* mutants, while apoptosis was only slightly increased (Fig. S4E-L), suggesting that the smaller brain width is due to a local distortion of the tissue rather than a decreased number of cells. Next, we quantitatively analysed the straightness of the brain/OP boundary. Note that the *Tg(eltC:GFP)* line could not be used for that purpose because a few cells in the OP also express the transgene. In addition, *Tg(cldnb:Gal4; UAS:RFP)* expression is mosaic in the OP, preventing the use of this line to assess the shape of the brain/OP boundary. To perform such a quantification we thus turned to immunostainings for *Dlx3b*, a transcription factor specifically expressed in OP (and skin) cells (Torres-Paz and Whitlock, 2014). We used deep learning to segment the 3D z-stacks of *Dlx3b*-immunostaining in control and *sly* mutant embryos at 36 hpf (Fig. 5E-F), and quantified the distortion of the OP/brain frontier at various z levels. This analysis demonstrated that the OP/brain boundary is less defined in *sly* mutants as compared with controls (Fig. 5G, H). Thus, our analyses of cell tracks, brain size and proliferation/apoptosis, and of the shape of the brain/OP boundary suggest that the forebrain is smaller and distorted in *sly* mutants due to the inward convergence of the two OPs. These findings reveal that the Laminin  $\gamma 1$ -dependent BMs serve to establish a straight brain/OP boundary preventing local intermixing and the late convergence of the two OPs towards each other during the flexure movement.

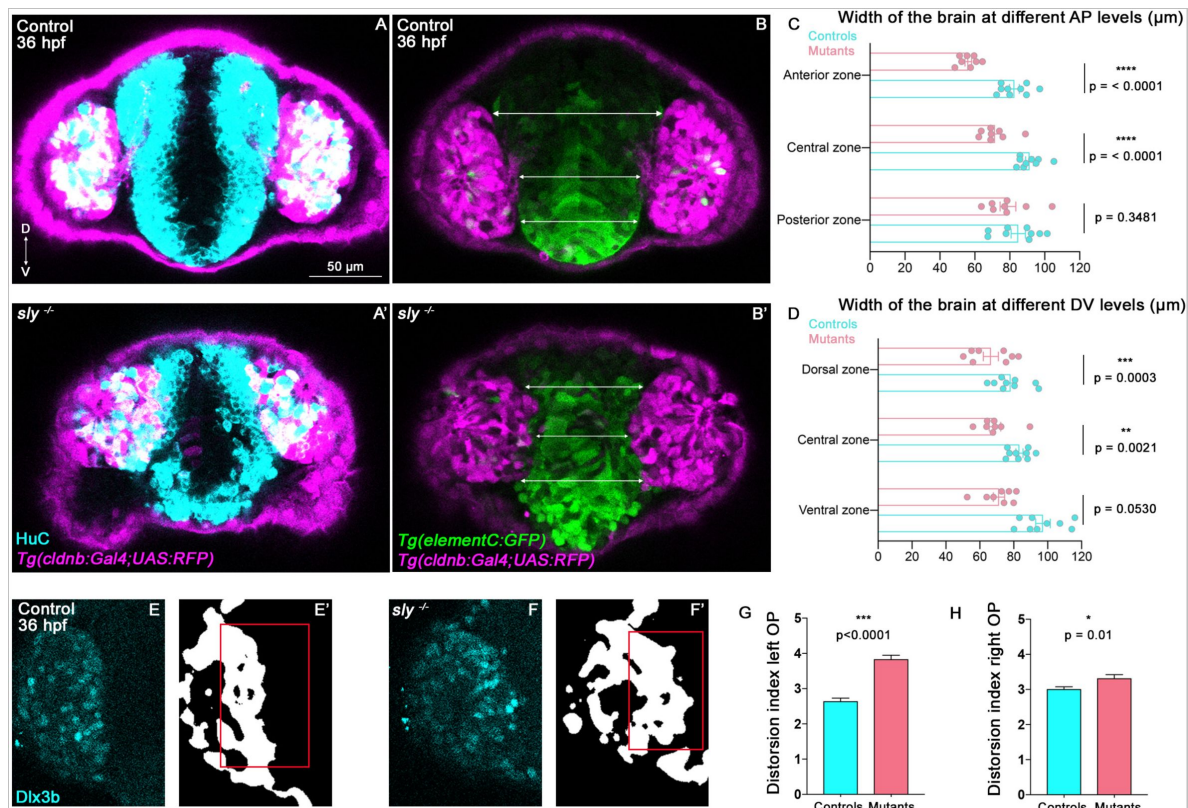


**Figure 5.**

### Analysis of brain width and brain/placode boundary in *sly* mutants and control siblings.

**A, A'.** Immunostaining for HuC (cyan) at 36 hpf on *Tg(cldnb:Gal4; UAS:RFP)* (magenta) control and *sly* mutant embryos (frontal view). Similar immunostainings performed at 28 hpf are shown in Fig. S4A, A'. **B, B'.** Images of *Tg(elementC:gfp); Tg(cldnb:Gal4; UAS:RFP)* control and mutant embryos at 36 hpf (frontal view), similar images acquired at 28 hpf are shown in Fig. S4B, B'. GFP (green) is expressed by the forebrain and a few OP cells. Arrows indicate where the brain width was measured (in 3 distinct positions along the DV axis). Measurements were also carried out at 3 distinct AP levels (through the z-stack). **C, D.** Width of the forebrain in 36 hpf controls and *sly* mutants, at 3 different DV and 3 different AP levels ( $n = 9$  controls and  $n = 8$  mutants from 4 independent experiments, unpaired, two-tailed t test). Quantifications for the 28 hpf stage are shown in Fig. S4C, D. **E–F'.** Immunostaining for the OP marker Dlx3b (cyan) was performed on 36 hpf *sly* mutants and control siblings (frontal view). The signal was segmented using deep learning approaches (white signal), and the distortion index (see Material and Methods) of the OP/brain boundary was calculated in the regions outlined with red boxes. **G, H.** Graphs showing the distortion indexes in controls and mutants at 36 hpf, for the left and right OPs ( $n = 3$  controls and  $n = 3$  mutants). ANOVA test (mixed models, with animals as random effect and genotype and side as fixed effects).



## Role of Laminin $\gamma$ 1-dependent BMs in olfactory axon development

The growth of the olfactory axons starts with the retrograde axon extension of their proximal portions during OP coalescence, from 14 to 22 hpf (Breau et al., 2017 [↗](#)), followed by the dorsal growth from the brain/OP boundary to the olfactory bulb from 22 to 32 hpf (Fig. 1K [↗](#)). Laminin has been reported to orient the emergence of axons (Randlett et al., 2011 [↗](#); Moore et al., 2022 [↗](#)). Do the Laminin  $\gamma$ 1-dependent BMs play any role in axon emergence or anchoring during retrograde axon extension? On fixed *Tg(omp:meYFP) sly* mutants at 24 hpf, numerous YFP+ neurons had their proximal axonal portion formed and attached to the brain surface (Fig. S5A-D), suggesting that retrograde axon extension occurs normally for at least some of the YFP+ OP neurons. Thus, the presence of a BM around the OP and/or the brain appears not to be an absolute requirement for the attachment of axon tips to the ventro-medial wall of the OP during retrograde extension.

Are Laminin  $\gamma$ 1-dependent BMs important for the growth or navigation of the axons from the brain/OP boundary to the olfactory bulb, as suggested by Laminin expression? We first examined the axons in *Tg(omp:meYFP)* embryos at 24, 28, 32 and 36 hpf. In mutant embryos, severe axonal defects were observed. Most YFP+ axonal protrusions were unable to leave the OP and appeared to stall at the OP/brain boundary (Fig. S5E, left column). In some embryos (8-10%), a small proportion of axons managed to reach the presumptive OB region by exiting the OP dorsally, while the axons would normally exit the OP at more ventral positions in the controls (Fig. S5E, left column and Movie 6). In addition, ectopic medial projections were observed in mutant embryos (18 to 30% of the embryos depending on the stage, as compared to 0 to 9% in controls, Fig. S5E, right column), suggesting navigation issues.

So far the growth of the zebrafish olfactory axons from the OP to the bulb has been mostly characterised using fixed samples or live imaging with long time intervals (Dynes and Ngai, 1998 [↗](#); Miyasaka et al., 2007 [↗](#)). To analyse the dynamic behaviour of the axons, we performed live imaging from 22 hpf on *sly* mutant and control embryos injected with the *omp:meYFP* plasmid, in order to obtain a mosaic labelling of the YFP+ neurons and their axons ( $n = 5$  mutants and  $n = 5$  controls, Fig. 6A, B [↗](#)). We tracked individual YFP+ growth cones, as well as the YFP+ cell bodies in the OP, during consecutive periods of 200 min each. We subtracted the average movement of OP cell bodies from the growth cone tracks, in order to remove the contribution of the global flexure remodelling and analyse specifically the behaviours of the axons with respect to the surrounding cells/tissue. In controls, as expected, growth cones overall showed a dorsal and medial migration, except at the end of the movie, which likely corresponds to their arrival and stalling in the presumptive olfactory bulb. By contrast, growth cones in the *sly* mutants did not display a directional migration towards the bulb (Fig. 6C, F, I, L [↗](#)). They were active and explored the environment, as shown by speed and persistence measurements, but moved on short distances and/or without preferential direction (Fig. 6C-N [↗](#)). These live imaging analyses confirm that the migration of the olfactory axons is drastically impaired in *sly* mutants, showing that Laminin  $\gamma$ 1-dependent BMs are essential for the growth and navigation of the axons from the OP to the olfactory bulb.

## *Sly* mutants display cranial NCC defects but this does not contribute to the late olfactory system phenotypes

Cranial NCC migration is concomitant with OP coalescence. From 14 hpf, they progressively populate the gaps between the OP and the eye and brain tissues (Harden et al., 2012 [↗](#); Torres-Paz and Whitlock, 2014 [↗](#); Bryan et al., 2020 [↗](#)). Our electron microscopy observations suggested that NCC are absent at the brain/OP interface of *sly* mutants. *In situ* hybridisation for the pan-NCC marker *crestin* (Luo et al., 2001 [↗](#)) revealed that, while a clear NCC cluster can be seen at the

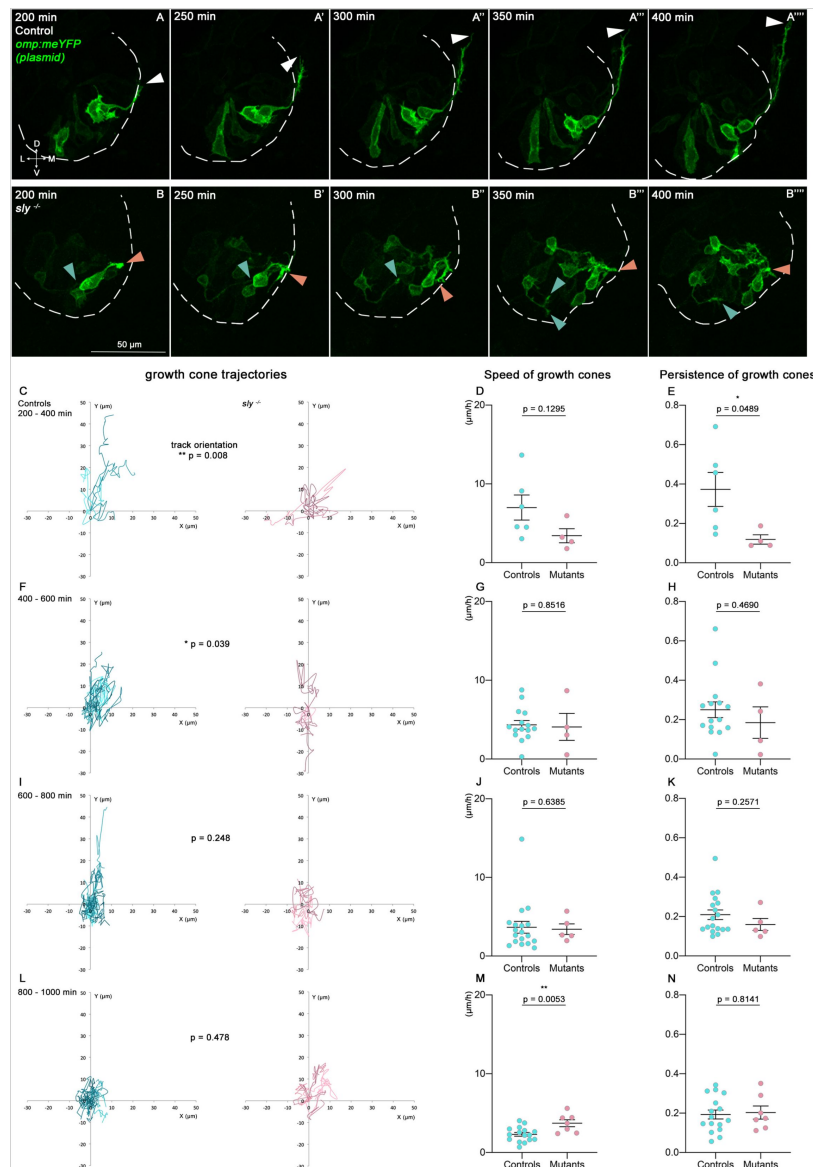


**Figure 6.**

### Quantitative live imaging of axonal behaviours in *sly* mutants and control siblings.

**A, B.** Images extracted from confocal live imaging on control (A-A''') and *sly* mutant (B-B''') embryos injected with the *omp:meYFP* plasmid to obtain a mosaic labelling of OP neurons and their axons (frontal view, maximum projections). The OP neurons and their axons were imaged over 1000 min from 22 hpf. Here, only the 200-400 min time window is shown as an example. Arrowheads = positions of individual growth cones over time. **C-N.** Individual YFP+ growth cones, as well as YFP+ cell bodies in the OP, were tracked during 4 consecutive periods of 200 min each (from 200 min of imaging, since before no growth cone could be detected,  $n = 5$  mutants and  $n = 5$  controls from 6 independent experiments). The mean movement of OP cell bodies was subtracted from the growth cone tracks to get rid of the global flexure movement. 200-400 min: 6 growth cones in controls, 4 in mutants; 400-600 min: 15 growth cones in controls, 4 in mutants; 600-800 min: 18 growth cones in controls, 4 in mutants; 800-1000 min: 16 growth cones in controls, 7 in mutants. **C, F, I, L.** Tracks of the growth cones merged at their origin for the 4 consecutive periods of 200 min. For each time window, the difference in the orientation of the tracks was analysed using the circular analysis of variance based on the likelihood ratio test. **D, G, J, M.** Mean speed of the growth cones. Unpaired, two-tailed t tests. **E, H, K, N.** Persistence of the growth cones, defined as the distance between the initial and final positions of the growth cones divided by the total length of their trajectory. Unpaired, two-tailed t tests, except for the analysis of the persistence at 400-600 min, and for the speed and persistence at 600-800 min, where Mann Whitney tests were performed.

brain/OP interface in controls at 32 hpf, *crestin*-labelled NCC are absent from this area in *sly* mutants (Fig. S6A, A'). This confirms that Laminin  $\gamma$ 1-dependent BMs are important for NCC migration or survival in this region of the embryo.

To test whether the phenotypes observed in *sly* mutants are linked to this NCC defect, we took advantage of the *foxd3* mutant, in which cranial NCC migration is delayed (Bryan et al., 2020 [↗](#); Monnot et al. 2022 [↗](#)), leading to a loss of *crestin*-labelled NCC at 32 hpf which resembles that of the *sly* mutants (Fig. S6B, B'). Importantly, Laminin expression appeared to be unchanged in *foxd3* mutants (Fig. S6C', D' and Monnot et al., 2022 [↗](#)). We previously showed that this mutant displays a slightly higher (of about 8-10  $\mu$ m) ML dimension of the OP at the end of coalescence (Monnot et al., 2022 [↗](#)) which is similar to what we observed in *sly* mutants (Fig. 3D [↗](#)). This suggests that the NCC defect could be the cause of the increased ML dimension in *sly* mutants. We hypothesize that in absence of NCC around the OP at this stage, the OP tissue is less constrained and thus slightly spread along the ML axis. To further investigate the influence of NCC on the development of the olfactory system at later stages, we analysed OP dimensions and the length of the olfactory axon bundle at 28 and 36 hpf, in *foxd3*<sup>-/-</sup> mutants and *foxd3*<sup>+/-</sup> or <sup>+/+</sup> control siblings expressing the *Tg(omp:meYFP)* transgene. No significant difference was observed between controls and *foxd3*<sup>-/-</sup> mutants for these parameters (Fig. S6C-L), suggesting that the late OP morphogenesis and axonal phenotypes of the *sly* mutants are not a consequence of the impairment of NCC development.

## Discussion

Our study highlights key roles of Laminin  $\gamma$ 1-dependent BMs in critical aspects of the development of the zebrafish olfactory system, revealed here through the detailed analysis of the Laminin  $\gamma$ 1 loss-of-function mutant *sly*. During the late development of the OP, Laminin  $\gamma$ 1-dependent BMs turned out to be essential to maintain its shape and proper position, and to establish a robust brain/placode boundary. In addition, Laminin-dependent BMs also appeared to be instrumental to ensure a proper growth and pathfinding of the olfactory axons towards the developing olfactory bulb. In the following paragraphs, we will discuss these new roles assigned to BMs in the context of the development of the zebrafish olfactory system, in light of the literature.

### The BM of the OP acts as a “shell” maintaining its shape and proper position in the face of forebrain flexure movements

Our data document a mild perturbation of cell movements during OP coalescence, which suggests that Laminin  $\gamma$ 1-dependent BMs are overall dispensable for the OP to acquire its initial shape. However, our observation that the OP of the *sly* mutant becomes significantly elongated in the DV dimension and is surrounded by ectopic cells during the forebrain flexure provides strong evidence for a role of the BMs in preventing OP deformation and scattering during this major remodelling of the head tissues. We discovered, along our live imaging observations, a joint anterior and ventral movement of the OPs and forebrain during the flexure time period in the control animals, as if the OPs were dragged along in the same antero-ventral movement as the forebrain. We thus propose that the BM of the OP prevents its deformation in response to the mechanical forces generated by the morphogenetic movement of the neighboring brain.

The ability of the placode's BM to limit the deformation of the OP during this developmental step most probably relies on its stiffness. In the *Drosophila* egg chamber, while Laminin itself has a minor contribution to the BM mechanical properties, Collagen IV, which deposition in the BM depends on Laminin (Díaz de la Loza et al., 2017 [↗](#)) has a major contribution to these properties, and in particular to its stiffness (Töpfer et al., 2022 [↗](#)). Actually, this BM is characterized by a gradient of stiffness, due to a gradient of Collagen IV, endowing the BM with anisotropic resistance to tissue expansion, allowing egg chamber elongation (Crest et al., 2017 [↗](#)). Even though the putative loss of mechanical properties leading to OP deformation observed in the *sly* mutant is

consecutive of a Laminin loss-of-function, it remains conceivable that it is the Collagen IV, rather than the Laminin itself, which is responsible of these mechanical properties in wild-type animals. This hypothesis, in line with the dramatic disorganization of the Collagen IV pattern observed by immunofluorescence in the *sly* mutant, however requires to be challenged by further investigation.

BMs were for long considered as inert and passive biological material, unable to generate forces by themselves. We now know that their composition is dynamic during morphogenesis (Díaz de la Loza et al., 2017 [↗](#); Harunaga et al., 2014 [↗](#); Khalilgharibi and Mao, 2021 [↗](#); Van De Bor et al., 2021 [↗](#)) and this dynamics has been proposed to generate autonomous stresses, i.e. within the BM itself (Loganathan et al., 2016 [↗](#); Pastor-Pareja and Xu, 2011 [↗](#); Zamir et al., 2008 [↗](#)). Accordingly, Serna-Morales et al. (Serna-Morales et al., 2023 [↗](#)) recently showed that the *Drosophila* ventral nerve cord morphogenesis is driven by a sudden increase in ECM-driven surface tension due to exponential assembly of Collagen IV in the BM. Still in *Drosophila*, it was recently shown that the elastic ECM enveloping the wing imaginal disc is a form of “active” shell whose anisotropic growth affects the tissue layers upon morphogenesis (Harmansa et al., 2023 [↗](#)). Whether such mechanisms participate to the control of the OP shape during the brain flexure remains to be addressed, through the analysis of the dynamics of expression of Collagen IV or other components of the BM as well as biomechanical investigations.

A dramatic consequence of the absence of proper OP and brain BMs in the *sly* mutant is the irregular and undefined frontier between the brain and OP, with placodal cells tending to locally intermingle with brain cells, and vice versa, along the OP/brain interface. This highlights a key role of these BMs in establishing a robust and straight boundary between the OP and the brain. Tissue intermixing has also been observed in the pharynx of Laminin mutants in *C. elegans* (Huang et al., 2003 [↗](#)) and in the *Xenopus* notochord upon loss-of-function of the Dystroglycan, a major Laminin receptor (Buisson et al., 2014 [↗](#)). The absence of a clear boundary between the OP and the brain in the *sly* mutant is accompanied by an apparent distortion of the brain, with notable reduced dimension in its medio-lateral axis. This phenotype, possibly due to the inward migration of the placodes that become partially embedded in the brain, illustrates an additional and unexpected role of the OP and brain BMs, in preventing late convergence of the two placodes towards each other during the flexure movement.

## BMs act as cues participating to the pathfinding of olfactory axons along their journey from the OP to the olfactory bulb

The early development of zebrafish olfactory axons begins with their retrograde extension, involving the attachment of the tips of the axonal protrusions to the brain's surface, followed by a lateral movement of the OP cell bodies in the opposite direction (Breau et al., 2017 [↗](#)). This initial step appears not to be affected in the *sly* mutant. These results suggest that Laminin-dependent BMs are dispensable for this retrograde axon extension and, more specifically, that Laminin  $\gamma$ 1 itself or other components of the BMs are unlikely to play a role in the anchoring of those axon tips onto the brain's surface, which is a prerequisite for their retrograde extension.

Our study shows that following retrograde elongation in the OP, the axons grow and navigate using bona fide growth cones, assemble a tight axon fascicle which crosses the BM of the OP, turns and migrates dorsally for a short distance between both BMs and thereafter crosses the brain BM to navigate towards the olfactory bulb. In other words, the olfactory axons have to cross two BMs. Our data show that the axons cross the first BM as it is still under construction and contain perforations, thus taking advantage of BM-free small pores to exit the OP and reach the narrow area located between the two BMs. By contrast, the entry point into the brain, across the second BM, opens with the arrival of the axons, suggesting that this opening is achieved by the axons themselves. It will be interesting, in future work, to determine whether the axons locally degrade



the BM through the secretion of matrix metalloproteases, or displace the BM with protrusive forces, or use a combination of both mechanisms (Chang and Chaudhuri, 2019 [DOI](#); Ihara et al., 2011 [DOI](#); Nazari et al., 2022 [DOI](#); Yamada et al., 2022 [DOI](#)).

As they migrate in the narrow corridor between the OP and brain BMs, olfactory axons remain confined in close proximity to the Laminin-rich BMs. Entering into the brain tissue, olfactory axons migrate collectively within a dynamic bundle growing towards the presumptive olfactory bulb. Importantly, once they have reached the brain tissue, the distalmost tip of this axon bundle still grows in close apposition to the internal surface of the brain's BM, suggesting that this BM serves as a migratory path promoting the growth of these axons. This hypothesis is reinforced by the fact that axon growth and directionality are dramatically impaired in the *sly* mutant, in which only few axons expressing *Tg(omp:meYFP)* can extend properly towards their target area. This phenotype is unlikely to be the result of defects in neuronal differentiation, as demonstrated by HuC immunolabeling and expression of the *Tg(neurog1:GFP)* and *Tg(omp:meYFP)* transgenes, which do not show obvious difference as compared to control animals, but appears to be rather due to axon growth and navigation defects. We did not formally identify the component(s) of the BM involved in this axon extension and pathfinding, but we consider Laminin itself as a good candidate for acting as a privileged substrate the axons, as Laminin does so for other populations of axons in zebrafish (Paulus and Halloran, 2006 [DOI](#); Semina et al., 2006 [DOI](#)), and has been shown in rodents to favor OSN axon extension *in vitro*, and to be present *in vivo* along the path followed by OSN axons from the olfactory epithelium to the bulb (Kafitz and Greer, 1997 [DOI](#)). From a molecular point of view, it has been established on cultured sympathetic neurons that Laminin accelerates the growth of axons through binding to integrins, which favors the formation of F-actin in the growth cone in a microtubule- and Rac1-dependent manner (Grabham et al., 2003 [DOI](#)). Recently, Abe et al. (2021) [DOI](#) further documented another role of Laminin in promoting hippocampal neuron growth cones enhanced progression on stiff substrate, through its interaction with L1, highlighting a new mechanosensitive axon outgrowth mediated by a L1-Laminin clutch mechanism (Abe et al., 2021 [DOI](#)). Whereas such Laminin-dependent mechanisms are used for guiding olfactory axons in zebrafish remains to be further explored. Other components of the BM, also affected in the *sly* mutant, may be involved as well in the regulation of olfactory axon development. Still in rodents indeed, the characterisation of the expression of ECM proteins along the developing olfactory pathway unraveled a complex interplay between ECM permissive and inhibitory cues expressed in a dynamic way, appearing to restrict axons to the pathway while promoting axon outgrowth within (Shay et al., 2008 [DOI](#)).

In addition to ECM molecules present in the BMs, guidance cues interacting with these molecules may also be involved in some aspects of the axonal defects observed in the *sly* mutant. For example, while *Xenopus* retinal axons are repulsed by ephrin-A5 on fibronectin, they are attracted by ephrin-A5 on Laminin (Weinl et al., 2003 [DOI](#)), and Laminin converts netrin-mediated attraction of these axons to repulsion (Höpker et al., 1999 [DOI](#)). Moreover, whereas slit2 repulses Robo expressing axons of dorsal root ganglia neurons, this repulsive effect is lost in absence of Laminin 111 (Nguyen-Ba-Charvet et al., 2001 [DOI](#)). Netrin1a and 1b are expressed in the zebrafish forebrain close to the route of the axons, where they play an attractive role for olfactory axons which express the netrin receptor DCC (Dang et al., 2023 [DOI](#); Lakhina et al., 2012 [DOI](#)). In addition, several ephrin and slits ligands are expressed in the forebrain at stages of axonal growth (zfin.org, Miyasaka et al., 2005 [DOI](#)). We may thus envisage that the absence of Laminin in the *sly* mutant may change in some way the netrin-, ephrin- or slit-dependent pathfinding of olfactory axons.

In conclusion, our findings indicate that the boundary between the sensory and central components of the olfactory system (Suter and Jaworski, 2019 [DOI](#)) is organised by the BMs of the OP and the brain. These BMs are permeable at specific locations to allow the sensory axons to enter the brain and use them as a substrate to grow towards the olfactory bulb, and at the same time

they maintain OP shape and position in the face of major morphogenetic movements occurring during the brain flexure, and ensure proper separation of the two tissues by preventing their intermixing.

## Material and Methods

### Zebrafish lines

Wild-type, transgenic and mutant zebrafish embryos were obtained by natural spawning. In the text, the developmental times in hpf indicate hours post-fertilization at 28.5°C. To obtain the 14–22 hpf stages, embryos were collected at 10 am, incubated for 2 h at 28°C before being placed overnight in a 23°C incubator to slow down development. Using this protocol, the embryos were at 14 hpf in the following morning at 10 am. We used the following lines (the simplified names are used in the figures and their legends): the zebrafish *sly*<sup>wi390</sup> (*sly/lamc1*) mutant (referred to as the *sly* mutant, [Wiellette et al., 2004](#) [DOI](#)), the *foxd3*<sup>zdf10</sup> mutant (referred to as the *foxd3* mutant, [Stewart et al., 2006](#) [DOI](#)), *Tg(-8.4neurog1:GFP)*<sup>sb1</sup> (referred to as *Tg(neurog1:GFP)*, [Blader et al., 2003](#) [DOI](#)) to label the early-born OP neurons at coalescence stages, *Tg(-2.0ompb:gapYFP)*<sup>rw032</sup> (a gift from Nobuhiko Miyasaka, RIKEN Institute, National Bioresource Project of Japan, referred to as *Tg(omp:meYFP)*, [Sato et al., 2007](#) [DOI](#)) to label *ompb*-expressing OP neurons and their axons from 22 hpf, *Tg(-4.0cldnb:GalTA4, cry:RFP)*<sup>nim11</sup> (referred to as *Tg(cldnb:Gal4)*, [Breau et al., 2013](#) [DOI](#)) combined with *Tg(14XUAS:mRFP,Xla.Cryg:GFP)*<sup>tp12</sup> (referred to as *Tg(UAS:RFP)*, [Balciuniene et al., 2013](#) [DOI](#)) to label all cells of the OP and their axons, *TgBAC(lamC1:lamC1-sfGFP)* ([Yamaguchi et al., 2022](#) [DOI](#)) to visualise the expression of LamC1-sfGFP under the control of the *lamC1* promoter, and *Tg(eltC:GFP)*<sup>zf199Tg</sup> (referred to as *Tg(elementC:gfp)*, [Stedman et al., 2009](#) [DOI](#)) to label the forebrain. All our experiments were made in agreement with the European Directive 210/63/EU on the protection of animals used for scientific purposes, and the French application decree “Décret 2013-118”. The fish facility has been approved by the French “Service for animal protection and health”, with the approval number A-75-05-25.

### Genotyping

The *sly*<sup>wi390</sup> mutant allele and the wild type locus were genotyped by PCR with the following primers: FW: 5'-CATGACGGCAAAGTTGGTGA-3'; RV1: 5'-CCATGCCTTGCAAAATGGCGTTA CTAA-3'; RV2: 5'-TGTAGGAGAGAAGTCGCGAG-3'. To detect the *sly*<sup>wi390</sup> allele (which is an insertion mutant allele, [Wiellette et al., 2004](#) [DOI](#)), the FW and RV1 were used to amplify a PCR product of 554 bp. The wild type allele was detected with the FW and RV2 primers to amplify a PCR product of 617 bp. The *foxd3*<sup>zdf10</sup> allele was genotyped with the CAPS (Cleaved Amplified Polymorphic Sequences) technique ([Neff et al., 2002](#) [DOI](#)) using the SspI restriction enzyme (NEB, R132S), as described in [Bryan et al., 2020](#) [DOI](#).

### Immunostainings

For Laminin, Nidogen and Collagen IV immunostainings, embryos were fixed in 4% paraformaldehyde (PFA, in PBS), dehydrated in methanol/PBS series and stored in methanol at -20°C. Embryos were rehydrated in methanol/PBS series, washed in PBS and treated with 10 µg/mL proteinase K (embryos at 24 hpf or younger: 1 min 30 s of incubation, later stages: 3 min of incubation). Embryos were then washed in glycine 2 mg/mL, post-fixed in 4% PFA and washed in PBS. For the other immunostainings, embryos were simply fixed in 4% PFA and washed in PBS. Embryos were then blocked in 3% goat serum and 0.3% triton in PBS for 2 h at room temperature or overnight at 4°C and incubated overnight at 4°C with primary and secondary antibodies.

The following primary antibodies were used: anti-Laminin (rabbit, 1/200, L-9393, Sigma), anti-Nidogen (rabbit, 1/200, ab14511, Abcam), anti-Collagen IV (rabbit, 1/200, ab6586, Abcam), anti-GFP (chicken, 1/200, GFP-1020, Aves labs), anti-DsRed (rabbit, 1/300, 632496, Takara), anti-phospho-

Histone H3 (rabbit, 1/200, 06-570, Millipore), anti-activated Caspase 3 (rabbit, 1/200, AF835, R and D systems), anti-HuC/D (mouse, 1/200, clone 16A11, A-21271, Thermofischer scientific) and anti-Dlx3b (mouse, 1/500, ZIRC).

## In situ hybridisation

Partial cDNA sequences for the NCC *crestin* marker were amplified by PCR using the 5'-AAGCCCTCGAAACTCACCTG-3' (FW) and 5'-CCACTTGATTCCCACGAGCT-3' (RV) primers. PCR products were subcloned in pGEM-T-easy (Promega) and sequenced. The Digoxigenin(DIG)-labelled riboprobe was synthesized from PCR templates. Embryos were fixed in 4% PFA in PBS and stored in methanol at -20 °C. Embryos were then rehydrated in methanol/PBS series, permeabilized 1 min 30 s with proteinase K (10 mg/ml), pre-hybridized, and hybridized overnight at 65 °C in hybridization mixture (50% formamide, 5 X standard saline citrate (SSC), 0.1% Tween 20, 100 µg/ml heparin, 100 µg/ml tRNA in water). The embryos were subjected to a series of washes in 50% SSC/formamide and SSC/PBST, and were then incubated in the blocking solution (0.2% Tween 20, 0.2% Triton X-100, 2% sheep serum in PBST) for one hour and overnight at 4 °C with alkaline phosphatase-conjugated anti-DIG antibodies (Roche) diluted at 1/4000 in the blocking solution. Embryos were then washed in PBST, soaked in staining buffer (TMN: 0.1M NaCl, 0.1M Tris-HCl, pH 9.5, 0.1% Tween 20 in water) and incubated in NBT/BCIP (nitroblue tetrazolium/5-bromo-4-chloro-3-indolyl phosphate) solution (Roche).

## Image acquisition

For live imaging, embryos were dechorionated manually and mounted at 14 hpf in 0.5% low melting agarose in 1X E3 medium. For movies on *Tg(neurog1:GFP)* embryos at coalescence stages, the embryos were imaged directly after the mounting, using a dorsal view, from 14 to 22 hpf. For movies on *Tg(omp:meYFP)* embryos, the embryos were placed at 33°C just after the mounting, and imaged from 22 hpf with a frontal view. Movies were recorded at 28.5°C on a Leica TCS SP8 MP11 upright multiphoton microscope using a 25X (numerical aperture (NA) 0.95) water lens. For fixed embryos, immunostained embryos were mounted in 0.5% low melting agarose in PBS and imaged on a Leica TCS SP5 AOBS upright confocal microscope using a 63X (NA 0.9) water lens or on a Zeiss 980 FAST Airyscan with a 20X (NA 1.0) water lens.

For electron microscopy, the zebrafish embryos were fixed in 2% glutaraldehyde and 2% PFA in 0.1M sodium cacodylate buffer pH 7.2 overnight at 4°C. Samples were washed in 0.1M cacodylate buffer, incubated for 1h in 1% osmium tetroxide in 0.1M cacodylate buffer, washed with deionized water, incubated 1h in 1% Uranyl Acetate and washed again with deionized water. To facilitate their orientation for sectioning, the zebrafish embryos were embedded in 4% agarose before being dehydrated through graded concentration of ethanol (50-70-95-100%). Samples were pre-embedded with graded concentration of anhydrous acetone and EPON epoxy resin mix (3:1 – 1:1 – 1:3) and embedded with 100% EPON. Finally, the embryos were mounted on silicon flat mold and polymerized at 60°C for 72 h. Ultrathin sections (80 nm) were prepared with an Ultracut ultramicrotome (UCT, Leica microsystems). They were deposited on silicon wafers, and contrasted with 2.5% uranyl acetate and 2% lead citrate. The wafers were stuck on aluminum stubs, plasma-cleaned, and observed at 1.5 kV, with a 30 µm aperture diameter and high current mode, at 2 mm WD, with SE and BSE in column detectors, in high vacuum in a Field-Emission SEM (Gemini 500, Zeiss). Images were automatically acquired with Atlas 5 (Fibics), with a pixel dwell time of 12.8 µs, a line averaging of 5, with a 8192 x 8192 definition and a pixel size fixed at 2.5 nm (corresponding to an image size of 20.5 × 20.5 µm), and an overlap of 16% between images. To obtain final mosaics, LookUp Table were inverted, SE and BSE signals were mixed, and manual stitching was made.

## Image analysis

### OP and brain dimensions

The ML dimension of the OP represents the distance between the most medial and the most lateral GFP+ or YFP+ cells in *Tg(neurog1:GFP)* or *Tg(omp:meYFP)* embryos, respectively. Ectopic fluorescent cells (cells that are physically separated from the main cluster) were not taken into account for this measurement. The same method was applied to quantify the AP and DV dimensions of the OP tissue. The width of the brain was measured along the ML axis using the GFP forebrain expression in *Tg(elementC:gfp)* embryos, at 3 different AP positions and 3 different DV positions.

### Thickness of the intercellular space in EM images

Analyses were performed on 1000 pixel-long rectangular regions at the interface between NCC and brain or OP cells in controls, and at the brain/OP interface in *sly* mutants (from 3 to 7 regions per embryo). In each region, the thickness of the intercellular space was manually measured every 100 pixels using Fiji (10 measurements/region). The average thickness per region and then per embryo was computed and plotted.

### Manual cell tracking

Individual cells from the OP (expressing *Tg(neurog1:GFP)* or *Tg(omp:meYFP)*) and the adjacent brain were tracked in 3D using the Manual Tracking plugin in ImageJ/Fiji. For tracking on *Tg(neurog1:GFP)* embryos, tracked cells from the brain and the OP expressed *Tg(neurog1:GFP)* at least at the end of the movie. For tracking on *Tg(omp:meYFP)* embryos, we followed forebrain cells located between the two OPs. For growth cone tracking, individual growth cones were followed in 3D using the same plugin in embryos injected with the *omp:meYFP* plasmid (Sato et al., 2005 [\[1\]](#)), over periods of 200 min each. The orientation of the trajectories represents the angle between the track and the vertical DV axis. 2D color coded trajectories and rose plots were generated in Matlab (Mathworks, US). The 3D MSD was computed using the Numpy library in Python (Harris et al., 2020 [\[2\]](#)). Plots representing cell tracks merged at their origin were produced with Microsoft Excel.

### Segmentation and analysis of the brain/OP boundary

The segmentation of Dlx3b+ OP cells was performed using a two-step workflow in Ilastik and Fiji softwares. First, to achieve pixel classification, 3 representative images of controls and of *sly* mutants were loaded into the data input menu and used to train the algorithm. After the training the pixel features and feature size (sigma) were selected. All features on all sigma scales were selected. This allowed pixels to be classified based on gray intensity, resemblance to an edge, and texture. Next, the supervised training was performed. 3 examples of each object were labelled; then, the classifier was allowed to update to observe the results. Using the uncertainty overlay, areas of high uncertainty were labeled iteratively until the prediction layer showed satisfactory identification of the pixels. This process was repeated for all 3 images. The trained classifier was then run on all images, and the pixel classification data were saved as segmented images. In the second step, a “region of interest” (ROI) containing the brain/OP boundary was manually defined using Fiji. The edge detection was applied in that ROI and allowed the delineation of the boundary between segmented OP cells and brain cells. The data were exported as CSV files to be used for analysis. The distortion index is defined as the total length of the boundary, divided by the distance between the dorsalmost and ventralmost positions along the analysed boundary region.



## Statistical analysis

Most graphs show means  $\pm$  standard error of the mean (sem), overlaid with all individual data points. These plots were generated with the GraphPad Prism software. For all graphs, we checked for normality of the data distribution before performing parametric, unpaired, two tailed t tests. When the data were not normal, a Mann-Whitney test was used. A Chi2 test was performed on the data presented in Fig. S2M-P and Fig. S4I-L. For the segmentation of the brain/OP boundary (Fig. 5G, H [↗](#)), the data were analyzed through an ANOVA test (mixed models, with animals as random effect and genotype and side as fixed effects). The orientation of cell and growth cone trajectories were treated as circular variables and analysed between groups using the circular analysis of variance based on the likelihood ratio test (Fig. 4O [↗](#) and Fig. 6C, F, I, L [↗](#)). The p values correspond to \*p < 0.05, \*\*p < 0.01, \*\*\*p < 0.001. No statistical method was used to estimate sample size and no randomization was performed.

## Acknowledgements

We gratefully acknowledge Jonathan Fouchard and Isabelle Bonnet for their help in image analysis, and Alexis Eschstruth for his help in molecular biology. This work was funded by the Agence Nationale pour la Recherche (ANR-17-CE13-0009-01 NEUROMECHANICS), the Centre National pour la Recherche Scientifique (CNRS), Sorbonne Université, and the National Institute of Health NIDCD Grant R01-DC-017989. We also thank the imaging platform of the Institut de Biologie Paris-Seine (the facility is supported by CNRS, Sorbonne Université and the Conseil Régional Ile-de-France), and the IBPS aquatic platform for fish care.

## Figure legends

**Figure S1. Electron microscopy analysis of intercellular spaces in the OP and brain tissues. A, A' and C, C'.** Examples of images of the intercellular space located between OP cells in control siblings (A, C) and in *sly* mutants (A', C'), at 24 and 32 hpf. Arrows = plasma membranes. **B, D.** Thickness of the intercellular space in the OP tissue in *sly* mutants and control siblings at 24 (n = 3 controls; n = 3 mutants) and 32 hpf (n = 2 controls; n = 3 mutants). Unpaired, two-tailed t test. **E, E' and G, G'.** Examples of images of the intercellular space located between brain cells in control siblings (A, C) and in *sly* mutants (A', C'), at 24 and 32 hpf. Arrows = plasma membranes. **F, H.** Thickness of the intercellular space in the brain tissue in *sly* mutants and control siblings at 24 (n = 3 controls; n = 3 mutants) and 32 hpf (n = 2 controls; n = 3 mutants). Unpaired, two-tailed t test.

**Figure S2. Analysis of proliferation and apoptosis in the OPs of *sly* mutants and control siblings. A-D'.** Immunostaining for Phospho-histone H3 (magenta) to label dividing cells on *Tg(neurog1:GFP)* embryos (green) at 16 hpf and 21 hpf (A-B' show images at 21 hpf, dorsal view), and on *Tg(omp:meYFP)* embryos (green) at 28 and 36 hpf (C-D' show images at 36 hpf, frontal view). In A-B' the OP is surrounded by a dotted line. Arrows = instances of Phospho-histone H3 positive cells in the placodal *Tg(neurog1:GFP)+* or *Tg(omp:meYFP)+* clusters. **E-H.** Number of Phospho-histone H3 positive cells in the OP at 16, 21, 28 and 36 hpf in control embryos and *sly* mutants. Unpaired, two-tailed t test. **I-L'.** Immunostaining for Activated Caspase 3 (magenta) to label apoptotic cells/debris on *Tg(neurog1:GFP)* embryos (green) at 16 hpf and 21 hpf (I-J' show images at 21 hpf, dorsal view), and on *Tg(omp:meYFP)* embryos (green) at 28 and 36 hpf (K-L' show images at 36 hpf, frontal view). In I-J' the OP is surrounded by a dotted line. Arrows = instances of Activated Caspase 3 positive cells or debris in the OP or in contact with the placodal *Tg(neurog1:GFP)+* or *Tg(omp:meYFP)+* clusters. **M-P.** % of OPs with zero, one or two and more Activated Caspase 3 positive cells or debris in the OP or very close to the OP at 16, 21, 28 and 36 hpf

in control embryos and *sly* mutants. Chi2 test. **Q, R.** Total number of YFP+ cells in control and mutant *Tg(omp:meYFP)*+ OPs at 28 hpf (Q) and 36 hpf (R) (n = 3 control placodes; n = 3 mutant placodes for each stage). Unpaired, two-tailed t test.

**Figure S3. Additional results on the OP morphogenesis defects observed in *sly* mutants. A-L.** Analysis of OP dimensions at 24, 28 and 32 hpf. **A, A', E, E' and I, I'.** Images (frontal views, 1 z-section) of representative OPs from *Tg(omp:meYFP)*; *sly*<sup>-/-</sup> mutants (right) and control *Tg(omp:meYFP)* siblings (left) at 24 (A, A'), 28 (E, E') and 32 hpf (I, I'). **B-D.** Graphs showing the AP, ML, and DV dimensions of the *Tg(omp:meYFP)*<sup>+</sup> OP clusters in *sly* mutants and control siblings at 24 hpf (n = 10 controls and n = 10 mutants from 3 independent experiments). Unpaired, two-tailed t test. **F-H.** Similar quantifications at 28 hpf (n = 13 controls and n = 10 mutants from 2 independent experiments). Unpaired, two-tailed t tests. **J-L.** Similar quantifications at 32 hpf (n = 17 controls and n = 13 mutants from 2 independent experiments). Unpaired, two-tailed t tests. Quantifications performed at 36 hpf are shown in **Fig. 4C-E**. **M, N.** Examples of 2D tracks plotted in a lateral view (AP along X and DV along Y) of *Tg(omp:meYFP)*<sup>+</sup> OP cells (red) and adjacent brain cells (green) in a control (M) and a *sly* mutant embryo (N). The time is color-coded: light colors at the beginning of the trajectory (22 hpf) towards dark colors for the end of the track (1080 min later).

Figure S4. Additional results for the analysis of brain shape and proliferation/apoptosis in *sly* mutants and control siblings. **A, A'.** Immunostaining for HuC (cyan) at 28 hpf performed on *Tg(cldnb:Gal4; UAS:RFP)* (magenta) control and *sly* mutant embryos (frontal view). Similar immunostainings performed at 36 hpf are shown in **Fig. 5A, A'**. **B, B'.** Images of *Tg(elementC:gfp)*; *Tg(cldnb:Gal4; UAS:RFP)* control and mutant embryos at 28 hpf (frontal view), similar images acquired at 36 hpf are shown in **Fig. 5B, B'**. GFP (green) is expressed by the forebrain, and a few OP cells. Arrows indicate where the thickness of the forebrain was measured (in 3 distinct positions along the DV axis). Measurements were also carried out at 3 distinct AP levels (through the z-stack). **C, D.** Width of the forebrain in 28 hpf controls and *sly* mutants, at 3 different DV and 3 different AP levels (n = 17 controls and n = 17 mutants from 5 independent experiments, unpaired, two-tailed t test). Quantifications for the 28 hpf stage are shown in **Fig. 5C, D**. **E-H.** Number of Phospho-histone H3 positive cells in the brain at 16, 21, 28 and 36 hpf in control embryos and *sly* mutants. Unpaired, two-tailed t test. **I-L.** % of embryos with zero, one or two and more Activated Caspase 3 positive cells or debris in the brain at 16, 21, 28 and 36 hpf in control embryos and *sly* mutants. Chi2 test.

**Figure S5. Additional results on olfactory axon development in *sly* mutants and control siblings. A-D.** Images (frontal view, 1 z-section) of representative OPs from *Tg(omp:meYFP)*; *sly*<sup>-/-</sup> mutant (C, D) and control *Tg(omp:meYFP)* siblings (A, B) at 24 hpf. Arrows = instances of proximal portions of the axons in the OP. **E.** Table describing the % of control and *sly* mutant embryos with a proper axonal bundle (1st column), with ventral projections (middle column) and with medial projections (right column) at 24, 28, 32 and 36 hpf. The numbers of embryos analysed at each stage are indicated in the table.

**Figure S6. NCC defects in *sly* mutants and olfactory system development in *foxd3* mutants. A, A'.** *In situ* hybridisation for the NCC marker *crestin* on 32 hpf controls and *sly* mutants. Arrowheads = *crestin*-positive NCC cluster at the OP/brain interface, which is absent in *sly* mutants. **B, B'.** *In situ* hybridisation for the NCC marker *crestin* on 32 hpf controls and *foxd3* mutants. Arrowheads = *crestin*-positive NCC cluster at the OP/brain interface, which is absent in *foxd3* mutants. **C, D.** Images (frontal view, maximum projection) of representative OPs of *Tg(omp:meYFP)*; *foxd3*<sup>-/-</sup> mutants and control siblings. **C', D'.** Laminin 111 immunostaining (1 z-section) on the same embryos. **E-H.** OP dimensions and length of the axon bundle at 28 hpf in *foxd3* mutants and control siblings (n = 31 controls and n = 13 mutants from 2 independent

experiments, unpaired, two-tailed t test). **I-L.** OP dimensions and length of the axon bundle in *foxd3* mutants and control siblings at 36 hpf (n = 21 controls and n = 4 mutants from 2 independent experiments, unpaired, two-tailed t test).

## Legends of the movies

**Movie 1. BM assembly around the brain and the OP during OP coalescence**, related to [Fig. 1](#). Same embryo as the z-section shown in [Fig. 1J](#). Confocal live imaging performed on a *TgBAC(lamC1:lamC1-sfGFP);Tg(cldnb:Gal4;UAS:RFP)* embryo in which Laminin  $\gamma$ 1-sfGFP is expressed under the control of its own promoter (green), and OP and peridermal skin cells are labelled in with cytoplasmic RFP (magenta). Pink arrowheads indicate the BM surrounding the brain, which is already assembled and continuous when the movie starts (at 17 hpf), while the BM surrounding the OP (shown with yellow arrowheads) assembles later, during OP coalescence. Grey dots indicate mesenchymal cells exhibiting Laminin  $\gamma$ 1-sfGFP cytoplasmic expression and migrating around the OP. Yellow dots indicate RFP-positive OP cells also showing Laminin  $\gamma$ 1-sfGFP cytoplasmic expression. Only the left side of the embryo is shown. One z-section, dorsal view, anterior to the top and lateral to the left, delta t = 10 min. Scale bar: 25  $\mu$ m.

**Movie 2. Formation of the exit and entry points in the BMs surrounding the OP and the brain**, related to [Fig. 1](#). Same embryo as the z-sections shown in [Fig. 1E-I](#). Confocal live-imaging performed on a *TgBAC(lamC1:lamC1-sfGFP);Tg(cldnb:Gal4;UAS:RFP)* embryo in which Laminin  $\gamma$ 1-sfGFP is expressed under the control of its own promoter (green), and OP and peridermal skin cells are labelled in with cytoplasmic RFP (magenta). The yellow arrowhead shows the exit point, which appears as a small interruption (or several small interruptions) in the BM of the OP resulting from its incomplete assembly in this specific area. The blue arrowhead indicates the opening of the entry point (which can also be formed by several gaps in some instances) in the already assembled BM of the brain, which is concomitant with the arrival of the RFP-positive axons. Pink dots indicate brain cells expressing Laminin  $\gamma$ 1-sfGFP cytoplasmic expression. Only the left side of the embryo is shown. One z-section, frontal view, dorsal to the top and lateral to the left, delta t = 10 min. Scale bar: 25  $\mu$ m.

**Movie 3. OP coalescence in a control embryo and a *sly* mutant**, related to [Fig. 3](#). Same embryos as the images and analyses shown in [Fig. 3F-I](#). Confocal live imaging showing OP coalescence movements in *sly* mutant and control *Tg(neurog1:GFP)* embryos, in which OP and brain neurons are labelled with cytoplasmic GFP. On the last time point, the dotted lines outline the OPs. Note that on the *sly* mutant movie, a marked drift movement occurs at t = 170 min, which has been taken into account and subtracted from the data in our cell tracking analysis. These embryos were injected with H2B-RFP mRNA to label nuclei and allow individual cell tracking (not shown). Average projection, dorsal view, anterior to the top, delta t = 10 min. Scale bar: 50  $\mu$ m.

**Movie 4. Behaviour of the OP neurons during the brain flexure movement in a control embryo and a *sly* mutant**, related to [Fig. 4](#). Same embryos as the images and analyses shown in [Figure 4I-L](#). Confocal live imaging showing OP cell movements and axon behaviours in *sly* mutant and control *Tg(omp:meYFP)* embryos, in which *ompb*-expressing OP neurons and their axons are labelled with membrane YFP. Note the global ventral movement occurring during the time-lapse, which corresponds to the movements of the OPs accompanying the brain flexure. These embryos were injected with H2B-RFP mRNA to label nuclei and allow individual cell tracking (not shown). Maximum projection, frontal view, dorsal to the top, delta t = 10 min. Scale bar: 50  $\mu$ m.

**Movie 5. 3D stacks showing the organisation of brain and OP neurons in control embryos and *sly* mutants**, related to [Fig. 5](#) and [Fig. S4](#). *sly* mutant and control *Tg(cldnb:Gal4;UAS:RFP)* embryos, in which OP and peridermal skin cells are labelled in with cytoplasmic RFP (magenta),

were immunostained for HuC (cyan) at 28 hpf and 36 hpf to visualise the neurons in the OP and the brain. Note that in control embryos, the frontier between the OP and the brain appears as a straight line whereas in mutant embryos, the boundary between the two tissues is not well defined, and the OPs appear to be partially embedded into the brain tissue. Frontal views, dorsal to the top, the first z-sections are the most anterior and the z-stack progressively goes posterior, z-step of 1  $\mu\text{m}$ . Scale bar: 50  $\mu\text{m}$ .

**Movie 6. 3D stacks showing the axonal defects and ectopic OP cells observed in *sly* mutants,** related to **Fig. 4** [↗](#) and Fig. S5. The embryos are at 28 hpf and carry the *Tg(omp:meYFP)* transgene to visualise the membrane of *ompb*-expressing OP neurons and their axons (green). In control embryos, the bundle of axons exit the OP in a ventral position and migrate dorsally towards the presumptive OB. In mutant embryos, only a few axons manage to exit the OP in a dorsal position and reach the presumptive OB (white arrow). Most of them appear to be stalled at the OP/brain boundary (grey arrow). The mutant embryo also exhibits ectopic OP cells that are detached from the main OP cluster (magenta dots). White dots indicate the centre of the rosette of OP neurons that assemble in the dorso-lateral region of the OP. Only the left side of the embryo is shown. Frontal views, dorsal to the top, lateral to the left, the first z-sections are the most anterior and the z-stack progressively goes posterior, z-step of 1  $\mu\text{m}$ . Scale bar: 25  $\mu\text{m}$ .



## References

- Abe K., Baba K., Huang L., Wei K. T., Okano K., Hosokawa Y., Inagaki N. (2021) **Mechanosensitive axon outgrowth mediated by L1-laminin clutch interface** *Biophys J* **120**:3566–3576
- Aguillon R., Madelaine R., Aguirrebengoa M., Guturu H., Link S., Dufourcq P., Lecaudey V., Bejerano G., Blader P., Batut J. (2020) **Morphogenesis is transcriptionally coupled to neurogenesis during peripheral olfactory organ development** *Development* **147**
- Anderson C., Thorsteinsdóttir S., Borycki A.G. (2009) **Sonic hedgehog-dependent synthesis of laminin alpha1 controls basement membrane assembly in the myotome** *Development* **136**:3495–504
- Balciuniene J., Nagelberg D., Walsh K. T., Camerota D., Georlette D., Biemar F., Bellipanni G., Balciunas D. (2013) **Efficient disruption of Zebrafish genes using a Gal4-containing gene trap** *BMC Genomics* **14**
- Baraban M., Gordillo Pi C., Bonnet I., Gilles J.-F., Lejeune C., Cabrera M., Tep F., Breau M. A. (2023) **Actomyosin contractility in olfactory placode neurons opens the skin epithelium to form the zebrafish nostril** *Dev Cell* **58**:361–375
- Belvindrah R., Hankel S., Walker J., Patton B. L., Müller U. (2007) **Beta1 integrins control the formation of cell chains in the adult rostral migratory stream** *J Neurosci* **27**:2704–2717
- Blader P., Plessy C., Strahle U. (2003) **Multiple regulatory elements with spatially and temporally distinct activities control neurogenin1 expression in primary neurons of the zebrafish embryo** *Mech Dev* **120**:211–8
- Bonner J., O'Connor T. P. (2001) **The permissive cue laminin is essential for growth cone turning in vivo** *J Neurosci* **21**:9782–9791
- Breau M. A., Wilkinson D. G., Xu Q. (2013) **A Hox gene controls lateral line cell migration by regulating chemokine receptor expression downstream of Wnt signaling** *Proc Natl Acad Sci U S A* **110**:16892–16897
- Breau M. A., Bonnet I., Stoufflet J., Xie J., De Castro S., Schneider-Maunoury S. (2017) **Extrinsic mechanical forces mediate retrograde axon extension in a developing neuronal circuit** *Nat Commun* **8**
- Breau M. A., Trembleau A. (2023) **Chemical and mechanical control of axon fasciculation and defasciculation** *Semin Cell Dev Biol* **140**:72–81
- Bryan C. D., Chien C. B., Kwan K. M. (2016) **Loss of laminin alpha 1 results in multiple structural defects and divergent effects on adhesion during vertebrate optic cup morphogenesis** *Dev Biol* **416**:324–37
- Bryan C. D., Casey M. A., Pfeiffer R. L., Jones B. W., Kwan K. M. (2020) **Optic cup morphogenesis requires neural crest-mediated basement membrane assembly** *Development* **147**

- Buisson N., Sirour C., Moreau N., Denker E., Le Bouffant R., Goullancourt A., Darribère T., Bello V. (2014) **An adhesome comprising laminin, dystroglycan and myosin IIA is required during notochord development in *Xenopus laevis*** *Development* **141**:4569–79
- Chang J., Chaudhuri O. (2019) **Beyond proteases: Basement membrane mechanics and cancer invasion** *J Cell Biol* **218**:2456–2469
- Chapman S. C., Sawitzke A. L., Campbell D. S., Schoenwolf G. C. (2005) **A three-dimensional atlas of pituitary gland development in the zebrafish** *J Comp Neurol* **487**:428–440
- Chen Z.-L., Haegeli V., Yu H., Strickland S. (2009) **Cortical deficiency of laminin gamma1 impairs the AKT/GSK-3beta signaling pathway and leads to defects in neurite outgrowth and neuronal migration** *Dev Biol* **327**:158–168
- Crest J., Diz-Muñoz A., Chen D. Y., Fletcher D. A., Bilder D. (2017) **Organ sculpting by patterned extracellular matrix stiffness** *Elife* **6**
- Dang P., Barnes D. T., Cheng R. P., Xu A., Moon Y. J., Kodukula S. S., Raper J. A. (2023) **Netrins and Netrin Receptors are Essential for Normal Targeting of Sensory Axons in the Zebrafish Olfactory Bulb** *Neuroscience* **508**:19–29
- Díaz de la Loza M. C., Díaz-Torres A., Zurita F., Rosales-Nieves A. E., Moeendarbary E., Franze K., Martín-Bermudo M. D., González-Reyes A. (2017) **Laminin Levels Regulate Tissue Migration and Anterior-Posterior Polarity during Egg Morphogenesis in *Drosophila*** *Cell Rep* **20**:211–223
- Dolez M., Nicolas J.-F., Hirsinger E. (2011) **Laminins, via heparan sulfate proteoglycans, participate in zebrafish myotome morphogenesis by modulating the pattern of Bmp responsiveness** *Development* **138**:97–106
- Dynes J. L., Ngai J. (1998) **Pathfinding of olfactory neuron axons to stereotyped glomerular targets revealed by dynamic imaging in living zebrafish embryos** *Neuron* **20**:1081–1091
- Garcia K. E., Okamoto R. J., Bayly P. V., Taber L. A. (2017) **Contraction and stress-dependent growth shape the forebrain of the early chicken embryo** *J Mech Behav Biomed Mater* **65**:383–397
- García-Alonso L., Fetter R. D., Goodman C. S. (1996) **Genetic analysis of Laminin A in *Drosophila*: extracellular matrix containing laminin A is required for ocellar axon pathfinding** *Development* **122**:2611–2621
- Grabham P. W., Reznik B., Goldberg D. J. (2003) **Microtubule and Rac 1-dependent F-actin in growth cones** *J Cell Sci* **116**:3739–3748
- Grant P. K., Moens C. B. (2010) **The neuroepithelial basement membrane serves as a boundary and a substrate for neuron migration in the zebrafish hindbrain** *Neural Dev* **5**
- Harden M. V., Pereiro L., Ramialison M., Wittbrodt J., Prasad M. K., McCallion A. S., Whitlock K. E. (2012) **Close association of olfactory placode precursors and cranial neural crest cells does not predestine cell mixing** *Dev Dyn* **241**:1143–54
- Harmansa S., Erlich A., Eloy C., Zurlo G., Lecuit T. (2023) **Growth anisotropy of the extracellular matrix shapes a developing organ** *Nat Commun* **14**

- Harris C. R. *et al.* (2020) **Array programming with NumPy** *Nature* **585**:357–362
- Harunaga J. S., Doyle A. D., Yamada K. M. (2014) **Local and global dynamics of the basement membrane during branching morphogenesis require protease activity and actomyosin contractility** *Dev Biol* **394**:197–205
- Hauptmann G., Gerster T. (2000) **Regulatory gene expression patterns reveal transverse and longitudinal subdivisions of the embryonic zebrafish forebrain** *Mech Dev* **91**:105–118
- Höpker V. H., Shewan D., Tessier-Lavigne M., Poo M., Holt C. (1999) **Growth-cone attraction to netrin-1 is converted to repulsion by laminin-1** *Nature* **401**:69–73
- Huang C.-C., Hall D. H., Hedgecock E. M., Kao G., Karantza V., Vogel B. E., Hutter H., Chisholm A. D., Yurchenco P. D., Wadsworth W. G. (2003) **Laminin alpha subunits and their role in C. elegans development** *Development* **130**:3343–3358
- Ihara S., Hagedorn E. J., Morrissey M. A., Chi Q., Motegi F., Kramer J. M., Sherwood D. R. (2011) **Basement membrane sliding and targeted adhesion remodels tissue boundaries during uterine-vulval attachment in Caenorhabditis elegans** *Nat Cell Biol* **13**:641–651
- Ivanovitch K., Cavodeassi F., Wilson S. W. (2013) **Precocious acquisition of neuroepithelial character in the eye field underlies the onset of eye morphogenesis** *Dev Cell* **27**:293–305
- Kafitz K. W., Greer C. A. (1997) **Role of laminin in axonal extension from olfactory receptor cells** *J Neurobiol* **32**:298–310
- Karamanos N. K., Piperigkou Z., Passi A., Götte M., Rousselle P., Vlodavsky I. (2021) **Extracellular matrix-based cancer targeting** *Trends Mol Med* **27**:1000–1013
- Karlstrom R. O. *et al.* (1996) **Zebrafish mutations affecting retinotectal axon pathfinding** *Development* **123**:427–438
- Kaur S., Kaur I., Rawal P., Tripathi D. M., Vasudevan A. (2021) **Non-matrigel scaffolds for organoid cultures** *Cancer Lett* **504**:58–66
- Khalilgharibi N., Mao Y. (2021) **To form and function: on the role of basement membrane mechanics in tissue development, homeostasis and disease** *Open Biol* **11**
- Kim S., Uroz M., Bays J. L., Chen C. S. (2021) **Harnessing Mechanobiology for Tissue Engineering** *Dev Cell* **56**:180–191
- Lakhina V., Marcaccio C. L., Shao X., Lush M. E., Jain R. A., Fujimoto E., Bonkowsky J. L., Granato M., Raper J. A. (2012) **Netrin/DCC signaling guides olfactory sensory axons to their correct location in the olfactory bulb** *J Neurosci* **32**:4440–4456
- Lee J., Gross J. M. (2007) **Laminin beta1 and gamma1 containing laminins are essential for basement membrane integrity in the zebrafish eye** *Invest Ophthalmol Vis Sci* **48**:2483–2490
- Li S., Liquari P., McKee K. K., Harrison D., Patel R., Lee S., Yurchenco P. D. (2005) **Laminin-sulfatide binding initiates basement membrane assembly and enables receptor signaling in Schwann cells and fibroblasts** *J Cell Biol* **169**:179–189
- Loganathan R., Rongish B. J., Smith C. M., Filla M. B., Czirok A., Bénazéraf B., Little C. D. (2016) **Extracellular matrix motion and early morphogenesis** *Development* **143**:2056–2065

- Luo R., An M., Arduini B. L., Henion P. D. (2001) **Specific pan-neural crest expression of zebrafish Crestin throughout embryonic development** *Dev Dyn* **220**:69–74
- Madelaine R., Garric L., Blader P. (2011) **Partially redundant proneural function reveals the importance of timing during zebrafish olfactory neurogenesis** *Development* **138**:4753–62
- Miner J. H., Yurchenco P. D. (2004) **Laminin functions in tissue morphogenesis** *Annu Rev Cell Dev Biol* **20**:255–284
- Miyasaka N., Sato Y., Yeo S.-Y., Hutson L. D., Chien C.-B., Okamoto H., Yoshihara Y. (2005) **Robo2 is required for establishment of a precise glomerular map in the zebrafish olfactory system** *Development* **132**:1283–1293
- Miyasaka N., Knaut H., Yoshihara Y. (2007) **Cxcl12/Cxcr4 chemokine signaling is required for placode assembly and sensory axon pathfinding in the zebrafish olfactory system** *Development* **134**:2459–2468
- Monnot P., Gangatharan G., Baraban M., Pottin K., Cabrera M., Bonnet I., Breau M. A. (2022) **Intertissue mechanical interactions shape the olfactory circuit in zebrafish** *EMBO Rep* **23**
- Moore R. E., Pop S., Alleyne C., Clarke J. D. W. (2022) **Microtubules are not required to generate a nascent axon in embryonic spinal neurons in vivo** *EMBO reports* **23**
- Nazari S. S., Doyle A. D., Yamada K. M. (2022) **Mechanisms of Basement Membrane Micro-Perforation during Cancer Cell Invasion into a 3D Collagen Gel** *Gels* **8**
- Neff M. M., Turk E., Kalishman M. (2002) **Web-based primer design for single nucleotide polymorphism analysis** *Trends Genet* **18**:613–615
- Nguyen-Ba-Charvet K. T., Brose K., Marillat V., Sotelo C., Tessier-Lavigne M., Chédotal A. (2001) **Sensory axon response to substrate-bound Slit2 is modulated by laminin and cyclic GMP** *Mol Cell Neurosci* **17**:1048–1058
- Odenthal J. *et al.* (1996) **Mutations affecting the formation of the notochord in the zebrafish, *Danio rerio*** *Development* **123**:103–115
- Parsons M. J., Pollard S. M., Saúde L., Feldman B., Coutinho P., Hirst E. M. A., Stemple D. L. (2002) **Zebrafish mutants identify an essential role for laminins in notochord formation** *Development* **129**:3137–3146
- Pastor-Pareja J. C., Xu T. (2011) **Shaping Cells and Organs in *Drosophila* by Opposing Roles of Fat Body-Secreted Collagen IV and Perlecan** *Developmental Cell* **21**:245–256
- Paulus J. D., Halloran M. C. (2006) **Zebrafish bashful/laminin-alpha 1 mutants exhibit multiple axon guidance defects** *Dev Dyn* **235**:213–224
- Pollard S. M., Parsons M. J., Kamei M., Kettleborough R. N. W., Thomas K. A., Pham V. N., Bae M.-K., Scott A., Weinstein B. M., Stemple D. L. (2006) **Essential and overlapping roles for laminin alpha chains in notochord and blood vessel formation** *Dev Biol* **289**:64–76
- Powell S. K., Kleinman H. K. (1997) **Neuronal laminins and their cellular receptors** *Int J Biochem Cell Biol* **29**:401–414



- Randlett O., Poggi L., Zolessi F. R., Harris W. A. (2011) **The oriented emergence of axons from retinal ganglion cells is directed by laminin contact in vivo** *Neuron* **70**:266–280
- Ross L. S., Parrett T., Easter S. S. (1992) **Axonogenesis and morphogenesis in the embryonic zebrafish brain** *J Neurosci* **12**:467–482
- Sato Y., Miyasaka N., Yoshihara Y. (2005) **Mutually exclusive glomerular innervation by two distinct types of olfactory sensory neurons revealed in transgenic zebrafish** *J Neurosci* **25**:4889–4897
- Sato Y., Miyasaka N., Yoshihara Y. (2007) **Hierarchical regulation of odorant receptor gene choice and subsequent axonal projection of olfactory sensory neurons in zebrafish** *J Neurosci* **27**:1606–1615
- Semina E. V., Bosenko D. V., Zinkevich N. C., Soules K. A., Hyde D. R., Vihtelic T. S., Willer G. B., Gregg R. G., Link B. A. (2006) **Mutations in laminin alpha 1 result in complex, lens-independent ocular phenotypes in zebrafish** *Dev Biol* **299**:63–77
- Serna-Morales E. *et al.* (2023) **Extracellular matrix assembly stress initiates Drosophila central nervous system morphogenesis** *Dev Cell* **58**:825–835
- Shay E. L., Greer C. A., Treloar H. B. (2008) **Dynamic expression patterns of ECM molecules in the developing mouse olfactory pathway** *Dev Dyn* **237**:1837–1850
- Sidhaye J., Norden C. (2017) **Concerted action of neuroepithelial basal shrinkage and active epithelial migration ensures efficient optic cup morphogenesis** *Elife* **6**
- Sittaramane V., Sawant A., Wolman M. A., Maves L., Halloran M. C., Chandrasekhar A. (2009) **The cell adhesion molecule Tag1, transmembrane protein Stbm/Vangl2, and Laminin alpha1 exhibit genetic interactions during migration of facial branchiomotor neurons in zebrafish** *Dev Biol* **325**:363–373
- Smyth N., Vatansever H. S., Murray P., Meyer M., Frie C., Paulsson M., Edgar D. (1999) **Absence of basement membranes after targeting the LAMC1 gene results in embryonic lethality due to failure of endoderm differentiation** *J Cell Biol* **144**:151–160
- Soleman S., Filippov M. A., Dityatev A., Fawcett J. W. (2013) **Targeting the neural extracellular matrix in neurological disorders** *Neuroscience* **253**:194–213
- Stedman A., Lecaudey V., Havis E., Anselme I., Wassef M., Gilardi-Hebenstreit P., Schneider-Maunoury S. (2009) **A functional interaction between Irx and Meis patterns the anterior hindbrain and activates krox20 expression in rhombomere 3** *Dev Biol* **327**:566–577
- Stemple D. L. *et al.* (1996) **Mutations affecting development of the notochord in zebrafish** *Development* **123**:117–128
- Stewart R. A., Arduini B. L., Berghmans S., George R. E., Kanki J. P., Henion P. D., Look A. T. (2006) **Zebrafish foxd3 is selectively required for neural crest specification, migration and survival** *Developmental Biology* **292**:174–188
- Suter T., Jaworski A. (2019) **Cell migration and axon guidance at the border between central and peripheral nervous system** *Science* **365**

- Theocharis A. D., Manou D., Karamanos N. K. (2019) **The extracellular matrix as a multitasking player in disease** *FEBS J* **286**:2830–2869
- Töpfer U., Guerra Santillán K. Y., Fischer-Friedrich E., Dahmann C. (2022) **Distinct contributions of ECM proteins to basement membrane mechanical properties in *Drosophila*** *Development* **149**
- Torres-Paz J., Whitlock K. E. (2014) **Olfactory sensory system develops from coordinated movements within the neural plate** *Dev Dyn* **243**:1619–31
- Torres-Paz J., Tine E. M., Whitlock K. E. (2021) **Dissecting the neural divide: a continuous neurectoderm gives rise to the olfactory placode and bulb** *Int J Dev Biol* **65**:275–287
- Tropepe V., Sive H. L. (2003) **Can zebrafish be used as a model to study the neurodevelopmental causes of autism?** *Genes Brain Behav* **2**:268–281
- Tsuda S. *et al.* (2010) **FAK-mediated extracellular signals are essential for interkinetic nuclear migration and planar divisions in the neuroepithelium** *J Cell Sci* **123**:484–496
- Urbano J. M., Torgler C. N., Molnar C., Tepass U., López-Varea A., Brown N. H., de Celis J. F., Martín-Bermudo M. D. (2009) ***Drosophila* laminins act as key regulators of basement membrane assembly and morphogenesis** *Development* **136**:4165–4176
- Van De Bor V., Loreau V., Malbouyres M., Cerezo D., Placenti A., Ruggiero F., Noselli S. (2021) **A dynamic and mosaic basement membrane controls cell intercalation in *Drosophila* ovaries** *Development* **148**
- Vöcking O., Van Der Meulen K., Patel M. K., Famulski J. K. (2023) **Zebrafish anterior segment mesenchyme progenitors are defined by function of *tfap2a* but not *sox10*** *Differentiation* **130**:32–42
- Walma D. A. C., Yamada K. M. (2020) **The extracellular matrix in development** *Development* **147**
- Weinl C., Drescher U., Lang S., Bonhoeffer F., Löschinger J. (2003) **On the turning of *Xenopus* retinal axons induced by ephrin-A5** *Development* **130**:1635–1643
- Whitlock K. E., Westerfield M. (1998) **A transient population of neurons pioneers the olfactory pathway in the zebrafish** *J Neurosci* **18**:8919–8927
- Whitlock K. E., Westerfield M. (2000) **The olfactory placodes of the zebrafish form by convergence of cellular fields at the edge of the neural plate** *Development* **127**:3645–53
- Wiellette E., Grinblat Y., Austen M., Hirsinger E., Amsterdam A., Walker C., Westerfield M., Sive H. (2004) **Combined haploid and insertional mutation screen in the zebrafish** *Genesis* **40**:231–240
- Wolman M. A., Sittaramane V. K., Essner J. J., Yost H. J., Chandrasekhar A., Halloran M. C. (2008) **Transient axonal glycoprotein-1 (TAG-1) and laminin-alpha1 regulate dynamic growth cone behaviors and initial axon direction in vivo** *Neural Dev* **3**
- Yamada K. M., Doyle A. D., Lu J. (2022) **Cell-3D matrix interactions: recent advances and opportunities** *Trends Cell Biol* **32**:883–895

## Article and author information

### P Tignard

Sorbonne Université, Centre National de la Recherche Scientifique (CNRS UMR7622), Institut de Biologie Paris-Seine (IBPS), Developmental Biology Laboratory, Paris, France, Sorbonne Université, Centre National de la Recherche Scientifique (CNRS UMR8246), Inserm U1130, Institut de Biologie Paris Seine (IBPS), Neuroscience Paris Seine (NPS), Paris, France

### K Pottin

Sorbonne Université, Centre National de la Recherche Scientifique (CNRS UMR7622), Institut de Biologie Paris-Seine (IBPS), Developmental Biology Laboratory, Paris, France  
ORCID iD: [0000-0001-9491-4660](https://orcid.org/0000-0001-9491-4660)

### A Geeverding

Imaging Facility, Institut de Biologie Paris-Seine (IBPS)  
ORCID iD: [0000-0002-0208-0302](https://orcid.org/0000-0002-0208-0302)

### M Doulazmi

Sorbonne Université, Centre National de la Recherche Scientifique (CNRS UMR8256), Institut de Biologie Paris Seine (IBPS), Adaptation Biologique et Vieillesse, Paris, France  
ORCID iD: [0000-0002-0313-1490](https://orcid.org/0000-0002-0313-1490)

### M Cabrera

Sorbonne Université, Centre National de la Recherche Scientifique (CNRS UMR7622), Institut de Biologie Paris-Seine (IBPS), Developmental Biology Laboratory, Paris, France  
ORCID iD: [0000-0002-2310-6284](https://orcid.org/0000-0002-2310-6284)

### C Fouquet

Sorbonne Université, Centre National de la Recherche Scientifique (CNRS UMR8246), Inserm U1130, Institut de Biologie Paris Seine (IBPS), Neuroscience Paris Seine (NPS), Paris, France

### M Liffra

Sorbonne Université, Centre National de la Recherche Scientifique (CNRS UMR8246), Inserm U1130, Institut de Biologie Paris Seine (IBPS), Neuroscience Paris Seine (NPS), Paris, France

### A Trembleau

Sorbonne Université, Centre National de la Recherche Scientifique (CNRS UMR8246), Inserm U1130, Institut de Biologie Paris Seine (IBPS), Neuroscience Paris Seine (NPS), Paris, France  
**For correspondence:** [alain.trembleau@sorbonne-universite.fr](mailto:alain.trembleau@sorbonne-universite.fr)  
ORCID iD: [0000-0002-8290-0795](https://orcid.org/0000-0002-8290-0795)

**MA Breau**

Sorbonne Université, Centre National de la Recherche Scientifique (CNRS UMR7622), Institut de Biologie Paris-Seine (IBPS), Developmental Biology Laboratory, Paris, France, Institut National de la Santé et de la Recherche Médicale (INSERM)

**For correspondence:** [marie.breau@sorbonne-universite.fr](mailto:marie.breau@sorbonne-universite.fr)

ORCID iD: [0000-0003-1884-7704](https://orcid.org/0000-0003-1884-7704)

**Copyright**

© 2023, Tignard et al.

This article is distributed under the terms of the [Creative Commons Attribution License](https://creativecommons.org/licenses/by/4.0/), which permits unrestricted use and redistribution provided that the original author and source are credited.

**Editors**

Reviewing Editor

**Emily Noël**

University of Sheffield, United Kingdom

Senior Editor

**Didier Stainier**

Max Planck Institute for Heart and Lung Research, Germany

**Reviewer #1 (Public Review):**

Summary:

The authors describe the dynamic distribution of laminin in the olfactory system and forebrain. Using immunohistochemistry and transgenic lines, they found that the olfactory system and adjacent brain tissues are enveloped by BMs from the earliest stages of olfactory system assembly. They also found that laminin deposits follow the axonal trajectory of axons. They performed a functional analysis of the sly mutant to analyse the function of laminin  $\gamma 1$  in the development of the zebrafish olfactory system. Their study revealed that laminin enables the shape and position of placodes to be maintained late in the face of major morphogenetic movements in the brain, and its absence promotes the local entry of sensory axons into the brain and their navigation towards the olfactory bulb.

Strengths:

-They showed that in the sly mutants, no BM staining of laminin and Nidogen could be detected around the OP and the brain. The authors then elegantly used electron microscopy to analyse the ultrastructure of the border between the OP and the brain in control and sly mutant conditions.

-To analyse the role of laminin  $\gamma 1$ -dependent BMs in OP coalescence, the authors used the cluster size of Tg(neurog1:GFP)+ OP cells at 22 hpf as a marker. They found that the mediolateral dimension increased specifically in the mutants. However, proliferation did not seem to be affected, although apoptosis appeared to increase slightly at a later stage. This increase could therefore be due to a dispersal of cells in the OP. To test this hypothesis, the authors then analysed the cell trajectories and extracted 3D mean square displacements (MSD), a measure of the volume explored by a cell in a given period of time. Their conclusion indicates that although brain cell movements are increased in the absence of BM during coalescence phases, overall OP cell movements occur within normal parameters and allow OPs to condense into compact neuronal clusters in sly mutants. The authors also analysed the dimensions of the clusters composed of OMP+ neurons. Their results show an increase in

cluster size along the dorso-ventral axis. These results were to be expected since, compared with BM, early neurog1+ neurons should compact along the medio-lateral axis, and those that are OMP+ essentially along the dorso-ventral axis. In addition to the DV elongation of OP tissue, the authors show the existence of isolated and ectopic (misplaced) YFP+ cells in sly mutants.

-To understand the origin of these phenotypes, the authors analysed the dynamic behaviour of brain cells and OPs during forebrain flexion. The authors then quantitatively measured brain versus OPs in the sly mutant and found that the OP-brain boundary was poorly defined in the sly mutant compared with the control. Once again, the methods (cell tracks, brain size, and proliferation/apoptosis, and the shape of the brain/OP boundary) are elegant but the results were expected.

-They then analysed the dynamic behaviour of the axon using live imaging. Thus, olfactory axon migration is drastically impaired in sly mutants, demonstrating that Laminin  $\gamma$ 1-dependent BMs are essential for the growth and navigation of axons from the OP to the olfactory bulb.

-The authors therefore performed a quantitative analysis of the loss of function of Laminin  $\gamma$ 1. They propose that the BM of the OP prevents its deformation in response to mechanical forces generated by morphogenetic movements of the neighbouring brain.

#### Weaknesses:

- The authors did not analyse neurog1 + axonal migration at the level of the single cell and instead made a global analysis. An analysis at the cell level would strengthen their hypotheses.

- Rescue experiments by locally inducing Laminin expression would have strengthened the paper.

-The paper lacks clarity between the two neuronal populations described (early EONs and late OSNs).

-The authors quantitatively measured brain versus OPs in the sly mutant and found that the OP-brain boundary was poorly defined in the sly mutant compared with the control. Once again, the methods (cell tracks, brain size, proliferation/apoptosis, and the shape of the brain/OP boundary) are elegant but the results were expected.

- A missing point in the paper is the effect of Laminin  $\gamma$ 1 on the migration of cranial NCCs that interact with OP cells. The authors could have analysed the dynamic distribution of neural crest cells in the sly mutant.

#### Reviewer #2 (Public Review):

##### Summary:

This manuscript addresses the role of the extracellular matrix in olfactory development. Despite the importance of these extracellular structures, the specific roles and activities of matrix molecules are still poorly understood. Here, the authors combine live imaging and genetics to examine the role of laminin gamma 1 in multiple steps of olfactory development. The work comprises a descriptive but carefully executed, quantitative assessment of the olfactory phenotypes resulting from loss of laminin gamma. Overall, this is a constructive advance in our understanding of extracellular matrix contributions to olfactory development, with a well-written Discussion with relevance to many other systems.

##### Strengths:

The strengths of the manuscript are in the approaches: the authors have combined live imaging, careful quantitative analyses, and molecular genetics. The work presented takes advantage of many zebrafish tools including mutants and transgenics to directly visualize the laminin extracellular matrix in living embryos during the developmental process.

##### Weaknesses:

The weaknesses are primarily in the presentation of some of the imaging data. In certain cases, it was not straightforward to evaluate the authors' interpretations and conclusions



based on the single confocal sections included in the manuscript. For example, it was difficult to assess the authors' interpretation of when and how laminin openings arise around the olfactory placode and brain during olfactory axon guidance.

**Reviewer #3 (Public Review):**

This is a beautifully presented paper combining live imaging and analysis of mutant phenotypes to elucidate the role of laminin  $\gamma$ 1-dependent basement membranes in the development of the zebrafish olfactory placode. The work is clearly illustrated and carefully quantified throughout. There are some very interesting observations based on the analysis of wild-type, laminin  $\gamma$ 1, and *foxd3* mutant embryos. The authors demonstrate the importance of a Laminin  $\gamma$ 1-dependent basement membrane in olfactory placode morphogenesis, and in establishing and maintaining both boundaries and neuronal connections between the brain and the olfactory system. There are some very interesting observations, including the identification of different mechanisms for axons to cross basement membranes, either by taking advantage of incompletely formed membranes at early stages, or by actively perforating the membrane at later ones.

This is a valuable and important study but remains quite descriptive. In some cases, hypotheses for mechanisms are stated but are not tested further. For example, the authors propose that olfactory axons must actively disrupt a basement membrane to enter the brain and suggest alternative putative mechanisms for this, but these are not tested experimentally. In addition, the authors propose that the basement membrane of the olfactory placode acts to resist mechanical forces generated by the morphogenetic movement of the developing brain, and thus to prevent passive deformation of the placode, but this is not tested anywhere, for example by preventing or altering the brain movements in the laminin  $\gamma$ 1 mutant.